ELECTRO-MAGNETIC PROPERTIES AND PHONONIC ENERGY DISSIPATION IN GRAPHENE BASED STRUCTURES

A THESIS
SUBMITTED TO THE DEPARTMENT OF PHYSICS
AND THE INSTITUTE OF ENGINEERING AND SCIENCE
OF BILKENT UNIVERSITY
IN PARTIAL FULFILLMENT OF THE REQUIREMENTS
FOR THE DEGREE OF
DOCTOR OF PHILOSOPHY

By
Hâldun Sevinçli
June 2008

I certify that I have read this thesis and that in my opinion it is fully adequate, in scope and in quality, as a dissertation for the degree of doctor of philosophy.

Prof. Salim Çıracı (Supervisor)

I certify that I have read this thesis and that in my opinion it is fully adequate, in scope and in quality, as a dissertation for the degree of doctor of philosophy.

Prof. M. Cemal Yalabık

I certify that I have read this thesis and that in my opinion it is fully adequate, in scope and in quality, as a dissertation for the degree of doctor of philosophy.

Prof. Bilal Tanatar

I certify that I have read this thesis and that in my opinion it is fully adequate, in scope and in quality, as a dissertation for the degree of doctor of philosophy.

Prof. Şakir Erkoç

I certify that I have read this thesis and that in my opinion it is fully adequate, in scope and in quality, as a dissertation for the degree of doctor of philosophy.

Prof. Engin U. Akkaya

Approved for the Institute of Engineering and Science:

Prof. Mehmet Baray,
Director of Institute of Engineering and Science

Abstract

ELECTRO-MAGNETIC PROPERTIES AND PHONONIC ENERGY DISSIPATION IN GRAPHENE BASED STRUCTURES

Hâldun Sevinçli
PhD in Physics
Supervisor: Prof. Salim Çıracı
June 2008

With the synthesis of a single atomic plane of graphite, namely graphene honeycomb structure, active research has been focused on the massless Dirac fermion behavior and related artifacts of the electronic bands crossing the linearly at the Fermi level. This thesis presents a theoretical study on the electronic and magnetic properties of graphene based structures, and phononic energy dissipation. First, functionalization of these structures by $3d$-transition metal (TM) atoms is investigated. The binding energies, electronic and magnetic properties have been investigated for the cases where TM-atoms adsorbed to a single side and double sides of graphene. It is found that $3d$-TM atoms can be adsorbed on graphene with binding energies ranging between 0.10 to 1.95 eV depending on their species and coverage density. Upon TM-atom adsorption graphene becomes a magnetic metal. TM-atoms can also be adsorbed to graphene nanoribbons with armchair edge shapes (AGNRs). Binding of TM-atoms to the edge hexagons of AGNR yield the minimum energy state for all TM-atom species examined in this work and in all ribbon widths under consideration. Depending

on the ribbon width and adsorbed TM-atom species, AGNR, a non-magnetic semiconductor, can either be a metal or a semiconductor with ferromagnetic or anti-ferromagnetic spin alignment. Interestingly, Fe or Ti adsorption makes certain AGNRs half-metallic with a 100% spin polarization at the Fermi level. These results indicate that the properties of graphene and graphene nanoribbons can be strongly modified through the adsorption of $3d$ TM atoms. Second, repeated heterostructures of zigzag graphene nanoribbons of different widths are shown to form multiple quantum well structures. Edge states of specific spin directions can be confined in these wells. The electronic and magnetic state of the ribbon can be modulated in real space. In specific geometries, the absence of reflection symmetry causes the magnetic ground state of whole heterostructure to change from antiferromagnetic to ferrimagnetic. These quantum structures of different geometries provide novel features for spintronic applications. Third, as a possible device application, a resonant tunnelling double barrier structure formed from a finite segment of armchair graphene nanoribbon with varying widths has been proposed based on first-principles transport calculations. Highest occupied and lowest unoccupied states are confined in the wider region, whereas the narrow regions act as tunnelling barriers. These confined states are identified through the energy level diagram and isosurface charge density plots which give rise to sharp peaks originating from resonant tunnelling effect. Finally, we studied dynamics of dissipation of local vibrations to the surrounding substrate. A model system consisting of an excited nano-particle which is weakly coupled with a substrate is considered. Using three different methods, the dynamics of energy dissipation for different types of coupling between the nano-particle and the substrate is studied, where different types of dimensionality and phonon densities of states were also considered for the substrate. Results of this theoretical analysis are verified by a realistic study. To this end the phonon modes and interaction parameters involved in the energy dissipation from an excited benzene molecule to the graphene are calculated performing first-principles calculations.

Keywords: graphene, graphene nanoribbons, spintronics, quantum transport, phononic dissipation.

Özet

GRAFEN TABANLI YAPILARDA ELEKTRONİK - MANYETİK ÖZELLİKLER VE FONONİK ENERJİ YİTİMİ

Hâldun Sevinçli
Fizik Doktora
Tez Yöneticisi: Prof. Salim Çıracı
Haziran 2008

Grafen olarak adlandırılan grafitin tek atom kalınlığındaki düzlemsel bal peteği yapısının sentezlenmesiyle kütlesiz Dirac fermiyonu davranışı ve Fermi seviyesini lineer olarak kesen elektronik bantların yolaçtığı etkiler aktif araştırmaların odağı haline geldiler. Bu tezde grafen tabanlı yapılarda elektronik ve manyetik özelliklerle fononik enerji yitimi teorik olarak incelenmiştir. İlk olarak grafen yapıların $3d$-geçiş elementleriyle (GE) işlevselleştirilmesi incelenmiştir. Bağlanma enerjileri, elektronik ve manyetik özellikler GE'lerin grafenin hem tek hem çift tarafına bağlandığı durumlar için hesaplanmış; bağlanma enerjilerinin GE'ye ve kaplama yoğunluğuna bağlı olarak 0.10 eV ile 1.95 eV arasında değiştiği bulunmuştur. Geçiş elementi bağlanmış grafen, manyetik metal özelliği göstermektedir. Geçiş elementlerinin 'armchair' kenar şekline sahip grafen nano-şeritlere (AGNŞ) bağlanması da incelenmiş; incelenen bütün şerit genişlikleri ve geçiş elementleri için en düşük enerjili durumun geçiş elementlerinin kenardaki altıgenlere bağlanmasıyla sağlandığı bulunmuştur. Çıplak hallerinde manyetik özelliği olmayan ve birer yarı-iletken olan AGNŞ'ler, GE bağlandığında şerit genişliği ve GE türüne bağlı olarak ferromanteyik veya

antiferromanyetik olabilmekte, metalize olabildikleri gibi yarı-iletken durumlarını koruyabilmektedirler. Bazı AGNŞ'ler Fe veya Ti bağlanmasıyla Fermi seviyesinde % 100 spin polarizasyonu göstererek yarı-metal özelliği kazanabilmektedirler. Bu sonuçlar grafen ve AGNŞ'lerin elektronik ve manyetik özellklerinin $3d$ GE bağlanmasıyla önemli değişiklikler gösterdiğini ortaya koymaktadır. İkinci olarak değişik kalınlıklara sahip zigzag kenar şekline sahip grafen nano-şeritlerin (ZGNŞ) periyodik olarak tekrarlanmasıyla oluşturulan hetero-yapıların çoklu kuvantum kuyuları oluşturduğu gösterilmiştir. Bu kuyularda farklı spin yönlerindeki kenar durumları hapsolabilmekte, dolayısıyla ZGNŞ'nin elektronik ve manyetik özellikleri gerçek uzayda değişimler gösterebilmektedir. Ayna simetrisinin varolmadığı geometrilerde ZGNŞ'nin taban durumu antiferromanyetikten ferrimanyetiğe dönüşmektedir. Değişik geometrilere sahip bu kuvantum yapılar spintronik uygulamalar için yeni bir zemin sunmaktadır. Üçüncü olarak, sonlu bir AGNŞ'nin kalınlığı modüle edilmiş, kuvantun taşınım hesaplamalarına dayanarak bu yapılarda çift bariyerli resonant tünelleme etkisinin varlığı gösterilmiş ve bu yapılar bir aygıt uygulaması olarak önerilmiştir. Dar kısımlar tünelleme bariyeri gibi davranarak en yüksek enerjili dolu seviye ile en düşük enerjili boş seviye kalın bölgeye hapsolmuştur. Enerji seviyesi diyagramı ve eşyoğunluk yüzey grafikleriyle tespit edilen hapsolmuş seviyeler iletkenlik grafiğinde sivri piklere sebep olmaktadır. Son olarak, yerel atomik titreşimlerin alttaşa yayılımının dinamiği incelenmiştir. Bir alttaş ve onunla zayıf olarak etkileşen uyarılmış bir nano-parçacıktan oluşan bir model sistem ele alınmış; üç farklı metod ile değişik etkileşim tipleri, alttaş için değişik boyutlar ve değişik fonon durum yoğunlukları farzedilerek enerji yitiminin dinamiği incelenmiştir. Bu analizlerin sonuçları uyarılmış bir benzen molekülünden grafen yüzeye enerji yitimini konu alan gerçekçi bir sistemde titreşim modları ve etkileşim sabitleri ilk prensiplerden hesaplanarak sınanmıştır.

Anahtar sözcükler: grafen, grafen nano-şeritler, spintronik, kuvantum taşınım, fononik enerji yitimi.

Acknowledgement

First of all I would like to express my sincere appreciation to my thesis supervisor Prof. Salim Çıracı for his most valuable guidance and support.

I should also express my honest thanks to the faculty members and the staff of the Physics Department and UNAM for providing a productive scientific environment throughout my studies.

I am thankful to my coauthors, the old and the new members of our research group.

I am gratefull to my friends at Bilkent without whom my years here would be boring.

I offer my sincere thankfulness to my family for their support.

And finally I am grateful to my wife Sevilay, to whom this thesis is dedicated, for sharing a life with me and for her encouragement and endless support in everything I do.

Contents

List of Figures

List of Tables

Chapter 1

Introduction

Carbon plays a unique role in nature by forming a number of very different structures. It is not only because it is capable of forming complex networks which are fundamental to organic chemistry, but also due to the seldom properties of its zero, one, two and three dimensional allotropes which are subjects of solid state physics. Its three dimensional structures (diamond and graphite) are known since ancient times, whereas the zero (fullerenes) and one dimensional (carbon nanotubes and linear atomic chains) are discovered within the last 10-20 years. The experimental observation of two dimensional carbon (graphene) has been accomplished only 4 years ago[1].

The two dimensional honeycomb structure of graphene plays a crucial role for understanding other graphitic forms (Fig. 1.1), and the electronic properties of graphene are governed by the binding characters of its orbitals. A σ-bond is formed between neighboring carbon atoms by sp^2 hybridization between one s-orbital and two p-orbitals. The remaining p-orbitals are perpendicular to the graphene plane and they form covalent bonds leading to a π-band.

Graphene is a zero band gap semiconductor (or a semimetal) with linear dispersion of bands near the Fermi level. This particular dispersion gives rise the lower energy excitations to behave as massless Dirac fermions with an effective speed of light $v_F \simeq 10^6$ m/s. Hence, at low energies, unusual properties of quantum electrodynamics are expected to be observed on graphene lattice. One

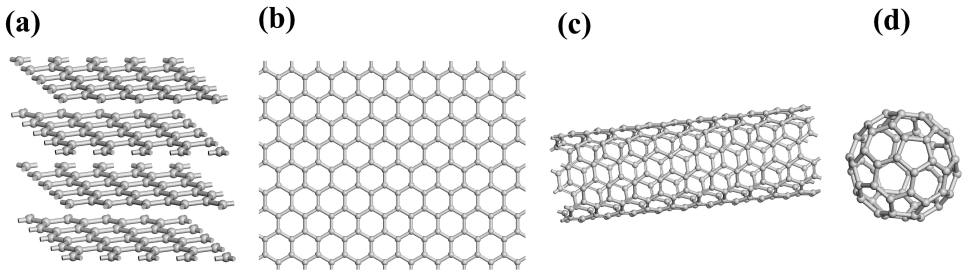

Figure 1.1: Graphitic carbon allotropes of three, two, one and zero dimensions, (a-d) respectively.

of the interesting features of Dirac fermions is the deterministic (unit probability) transmission through tunneling barriers of arbitrary width and height when incident normally. This counterintuitive property of ultra-relativistic particles, the so-called Klein paradox, is attributed only to exotic phenomena such as black hole evaporation, and graphene is expected to serve as a basis to verify our theories [2].

Besides its unusual basic properties, graphene is a candidate for a large number of applications and has the potential to offer new concepts in materials research and fundamental science [3, 4]. A variety of methods have been proposed or demonstrated in order to functionalize graphene based materials for new device applications [5–13] such as gas sensors [5], spin-valve devices [6–10], transistors [11, 12] and resonant tunneling devices [13].

The organization of the thesis is as follows. In the following sections of this chapter the basic electronic and magnetic properties of graphene and and its ribbons are summarized. Chapter 2 consists of three sections in which electromagnetic properties of graphene based structures are investigated upon transition metal atom adsorption, spin confinement at zigzag graphene nanoribbons is studied, and the resonant tunneling effect is illustrated for armchair graphene nanoribbons. In Chapter 3, methods and results of our study on dynamics of phonon discharge from a nano-particle weakly coupled to a substrate are discussed. A summary of the results and the conclusions are

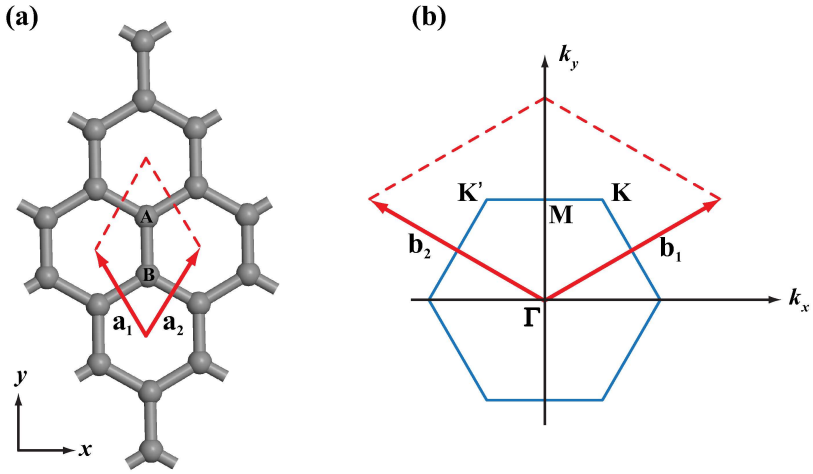

Figure 1.2: (a) The lattice structure and the unit cell vectors of graphene. A and B atoms belong to different sublattices. (b) The corresponding Brillouin zone and the special k-points $\mathbf{\Gamma}$, $\mathbf{M}$, $\mathbf{K}$ and $\mathbf{K}'$.

presented in Chapter 4.

1.1 Basic Electronic Properties of Graphene

The hexagonal lattice of graphene and its reciprocal lattice are shown in Fig. 1.2(a) and (b). The lattice vectors are

$$\mathbf{a}_1 = \frac{a}{2}\left(\sqrt{3}, 3\right), \qquad \mathbf{a}_2 = \frac{a}{2}\left(-\sqrt{3}, 3\right), \tag{1.1}$$

$a = 1.42$ Å being the nearest neighboor distance. Correspondingly, the reciprocal lattice vectors are:

$$\mathbf{b}_1 = \frac{2\pi}{3a}\left(\sqrt{3}, 1\right), \qquad \mathbf{b}_2 = \frac{2\pi}{3a}\left(-\sqrt{3}, 1\right), \tag{1.2}$$

The corners of the first Brillouin zone, $\mathbf{K}$ and $\mathbf{K}'$,

$$\mathbf{K} = \frac{2\pi}{3a}\left(\frac{1}{\sqrt{3}}, 1\right), \qquad \mathbf{K}' = \frac{2\pi}{3a}\left(-\frac{1}{\sqrt{3}}, 1\right), \tag{1.3}$$

are of particular importance for the physics of graphene. These points are called the Dirac points close to which the energy dispersion becomes linear as it will be discussed below.

The tight binding Hamiltonian has the simple form

$$H_{TB} = -t \sum_{\langle i,j \rangle \sigma} \left(a^{\dagger}_{i\sigma} b_{j\sigma} + H.c. \right) \tag{1.4}$$

where $a^{\dagger}_{i\sigma}$ ($a_{i\sigma}$) creates (annihilates) an electron on site $\mathbf{R}_i$ with spin σ on the A sublattice, and $b^{\dagger}_{j\sigma}$ ($b_{j\sigma}$) creates (annihilates) an electron on site $\mathbf{R}_j$ with spin σ on the B sublattice. The nearest neighboor ($\langle i,j \rangle$) hopping energy is $t \simeq 2.7$ eV [14]. The energy bands derived from this Hamiltonian have the form

$$E_{\pm}\mathbf{k} = \pm t \sqrt{3 + f(\mathbf{k})} \tag{1.5}$$

with

$$f(\mathbf{k}) = 2\cos\left(\sqrt{3}k_x a\right) + 4\cos\left(\frac{\sqrt{3}}{2}k_x a\right)\cos\left(\frac{3}{2}k_y a\right) \tag{1.6}$$

where the plus sign applies to π-, and the minus sign to the π^*-bands. Evidently, the above bands satisfy electron-hole symmetry by being symmetric around the zero of the energy. The full band structure of graphene obtained from the tight-binding Hamiltonian is shown in Fig. 1.3(a). In Fig. 1.3(b) a zoom in of the band structure to one of the Dirac points is shown. Fig. 1.3(d) and (e) show the band structure from two special view points.

The energy dispersions $E_{\pm}(\mathbf{k})$ can be expanded around $\mathbf{K}$ (or $\mathbf{K}'$) with $\mathbf{k} = \mathbf{K} + \mathbf{q}$ where $|\mathbf{q}| \ll |\mathbf{K}|$ by using $f(\mathbf{k}) \simeq -3 + 9a^2(q_x^2 + q_y^2)/4$ as

$$E_{\pm} = \pm \hbar v_F |\mathbf{q}| + \mathcal{O}\left[\left(\frac{q}{K}\right)^2\right]. \tag{1.7}$$

Here, the Fermi velocity is $v_F = 3ta/2\hbar$. In contrast to the the usual case where $v = \sqrt{2E/m}$, the Fermi velocity of low energy electrons of graphene do not depend on energy or momentum, which is the source of unusual effects.

Accordingly, the tight-binding Hamiltonian within the nearest neighboor approximation can be expressed in Dirac form by expanding the creation,

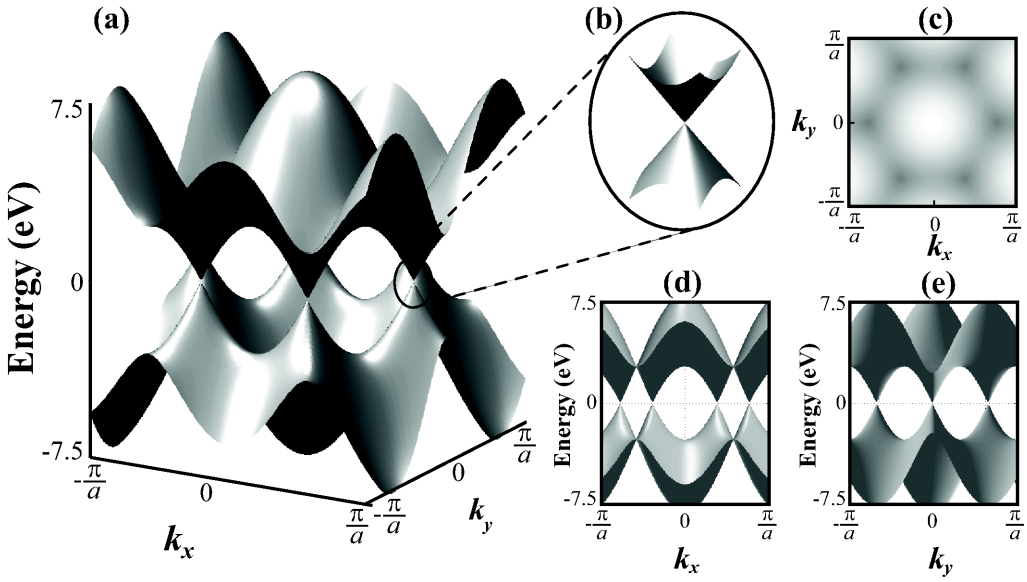

Figure 1.3: The full band structure of graphene for $-\pi/a < k_x, k_y < \pi/a$ (a), and a zoom in of the band structure close to one of the Dirac points (b). (c) Two dimensional map of the conduction band. Darker regions indicate lower energy. (d-e) The full band structure from special view points corresponding to the band structures along the k_x-- and k_y-directions. The $x-$direction can be named as the zigzag direction, and the k_y-direction as the armchair direction in accordance with Fig. 1.2(a). [see also Fig.1.5 and Fig. 1.6]

annihilation operators around the zero energy points[15]. Near the Fermi energy, the Fourier transform of the annihilation operator, $a_i = 1/\sqrt{N}\sum_{\mathbf{k}} e^{-i\mathbf{k}\cdot\mathbf{R}_i} a_{\mathbf{k}}$, collects the major contributions from $\mathbf{K}$ and $\mathbf{K}'$, N being the number of atoms per unit cell. So the annihilation operators can be simplified as

$$a_i \simeq e^{-i\mathbf{K}\cdot\mathbf{R}_i} a_{\mathbf{K}} + e^{-i\mathbf{K}'\cdot\mathbf{R}_i} a_{\mathbf{K}'}, \tag{1.8}$$

$$b_j \simeq e^{-i\mathbf{K}\cdot\mathbf{R}_j} b_{\mathbf{K}} + e^{-i\mathbf{K}'\cdot\mathbf{R}_j} b_{\mathbf{K}'}, \tag{1.9}$$

and writing $\Psi^\dagger_{\mathbf{K}} = \begin{pmatrix} a^\dagger_{\mathbf{K}} & b^\dagger_{\mathbf{K}} \end{pmatrix}$ one arrives at the Hamiltonian

$$H = -i\hbar v_F \int dx\, dy \left(\Psi^\dagger_{\mathbf{K}}(\mathbf{r}) \vec{\sigma} \cdot \nabla \Psi_{\mathbf{K}}(\mathbf{r}) + \Psi^\dagger_{\mathbf{K}'}(\mathbf{r}) \vec{\sigma}^* \cdot \nabla \Psi_{\mathbf{K}'}(\mathbf{r}) \right), \tag{1.10}$$

where $\vec{\sigma} = (\sigma_x, \sigma_y)$ and $\vec{\sigma}^* = (\sigma_x, -\sigma_y)$ are Pauli matrices. This Hamiltonian describes energy dispersions at two valleys around $\mathbf{K}$ and $\mathbf{K}'$ with $H_{\mathbf{K}}(\mathbf{k}) = \hbar v_F \vec{\sigma} \cdot \mathbf{k}$ and $H_{\mathbf{K}'}(\mathbf{k}) = \hbar v_F \vec{\sigma}^* \cdot \mathbf{k}$. One should note that the pseudo-spin variable associated with the two components of the spinor wavefunction stands for chirality, and the above Hamiltonian is valid only close to the Dirac points $\mathbf{K}$ and $\mathbf{K}'$. At low energies or in the presence of a finite energy band gap due to geometrical effects, validity of the Dirac Hamiltonian should be questioned.

1.2 Basic Electromagnetic Properties of Graphene Nanoribbons

The electronic structure and magnetic properties of graphene nanoribbons (GNRs) are primarily determined by their edge shapes and their widths [16–20]. Their electronic structures also depend on whether the dangling bonds of the edge atoms are passivated or not. In this thesis, all the GNRs considered are those passivated with hydrogen. In Fig. 1.4 (a) and (b) the lattice structures and the unit cells of GNRs with armchair and zigzag edge shapes are shown respectively. We denote GNRs having armchair edge shape with N_a dimer lines as AGNR(N_a), and those having zigzag edge shape with N_z zigzag chains as ZGNR(N_z).

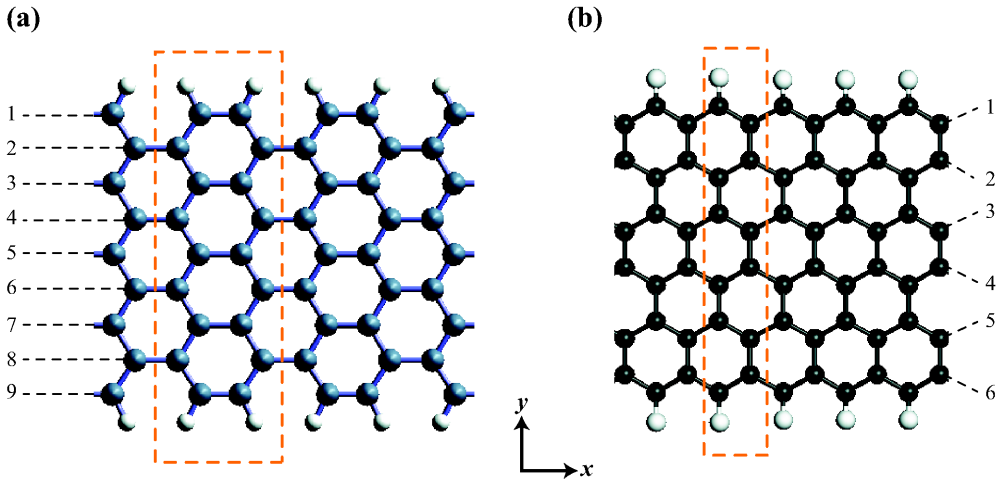

Figure 1.4: Lattice structures of (a) AGNR(9) and (b) ZGNR(6). Unit cells of the structures are delineated. The number $N_a = 9$ stands for the number of dimer lines while $N_z = 6$ stands for the number of zigzag chains along the $x-$direction.

Density functional theory[21] (DFT) calculations show that AGNRs are direct band gap semiconductors and that their band gaps follow three curves depending on their width, namely N_a [9]. For a given nonnegative integer n, $N_a = 3n + 1$ yields the highest band gap whereas $N_a = 3n - 1$ yields the lowest, $N_a = 3n$ lying in between as shown in Fig. 1.5. As n increases, all three curves approach to zero without crossing.

Even though tight-binding calculations predict a zero band gap for all ZGNRs [e.g. Fig. 1.6(a)], DFT calculations show that all ZGNR are semiconductors and their band gaps decrease monotonically with N_z, for $N_z > 4$. For all N_z values the highest valence band and the lowest conduction band give rise to a high density of states near the Fermi energy. The states causing this high value of density of states are localized at the edges of the ZGNR and this causes a magnetic transition. Eventually, it is possible to express this magnetic transition by adding an on-site Hubbard term to the tight-binding Hamiltonian as

$$H = -t \sum_{\langle i,j\rangle,\sigma} \left(a^{\dagger}_{i\sigma} b_{j\sigma} + H.c. \right) + U \sum_{i} \left(a^{\dagger}_{i\sigma} a_{i\sigma} a^{\dagger}_{i\sigma'} a_{i\sigma'} + b^{\dagger}_{i\sigma} b_{i\sigma} b^{\dagger}_{i\sigma'} b_{i\sigma'} \right) \qquad (1.11)$$

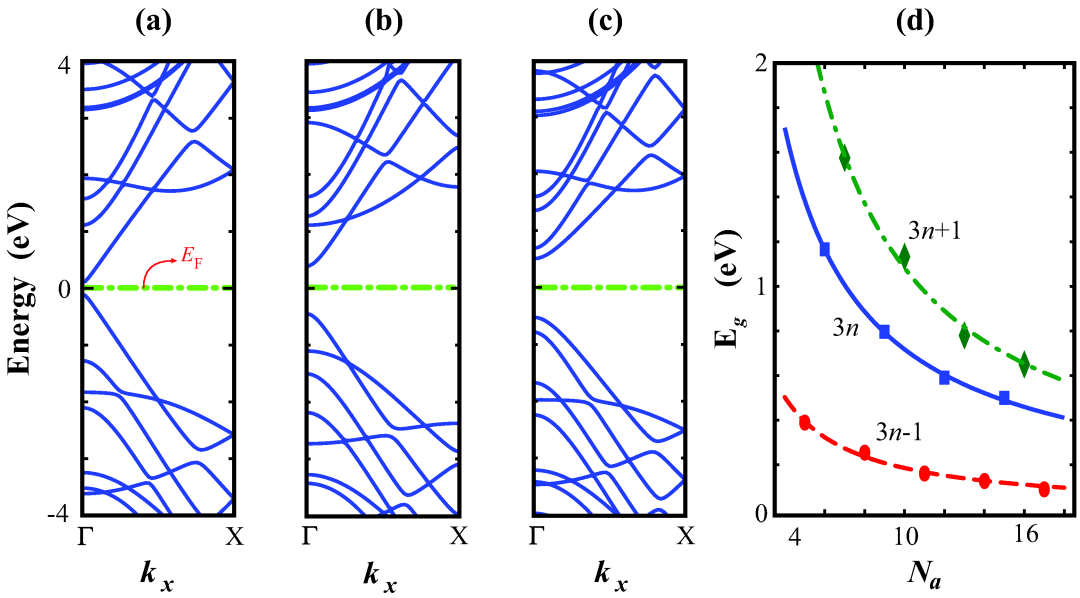

Figure 1.5: Band structures of AGNRs belonging to different families: (a) $N_a = 3n - 1 = 8$, (b) $N_a = 3n = 9$, and (c) $N_a = 3n + 1 = 10$. (d) Band gaps of the families as a function of N_a. Band structures are obtained using plane-wave DFT calculations, zero of the energy is set to E_F.

where U is the on-site repulsion energy [16].

This Hamiltonian can be solved in the mean field approximation numerically where the Hamiltonian is written in the form

$$H = -t \sum_{\langle i,j\rangle,\sigma} \left(a^{\dagger}_{i\sigma} b_{j\sigma} + H.c. \right) + U \sum_{i} \Big(\langle a^{\dagger}_{i\sigma} a_{i\sigma} \rangle a^{\dagger}_{i\sigma'} a_{i\sigma'} + a^{\dagger}_{i\sigma} a_{i\sigma} \langle a^{\dagger}_{i\sigma'} a_{i\sigma'} \rangle + \\ + \langle b^{\dagger}_{i\sigma} b_{i\sigma} \rangle b^{\dagger}_{i\sigma'} b_{i\sigma'} + b^{\dagger}_{i\sigma} b_{i\sigma} \langle b^{\dagger}_{i\sigma'} b_{i\sigma'} \rangle - \langle a^{\dagger}_{i\sigma} a_{i\sigma} \rangle \langle a^{\dagger}_{i\sigma'} a_{i\sigma'} \rangle - \langle b^{\dagger}_{i\sigma} b_{i\sigma} \rangle \langle b^{\dagger}_{i\sigma'} b_{i\sigma'} \rangle \Big) . \quad (1.12)$$

Starting with an initial guess for the spin occupations, $\langle a^{\dagger}_{i\sigma} a_{i\sigma} \rangle$ and $\langle b^{\dagger}_{i\sigma} b_{i\sigma} \rangle$, the Hamiltonian is solved and the spin occupations are recalculated to be used as the initial guess for the next iteration. These iterations are repeated until the initial occupations are no different than the calculated occupations and this calculation procedure is employed for each k-point in the reciprocal space.

While the tight binding solution of the ZGNR Hamiltonian in the absence of Hubbard term yields a zero band gap semiconductor, upon inclusion of the Hubbard term ZGNR is found to be a direct band gap semiconductor [Fig. 1.6(b)] with edge states localized at the opposite edges having opposite spins. Such a magnetic solution of the Hubbard Hamiltonian for bipartite lattices was previously proved by Lieb [22], and these results are also verified by DFT calculations as shown in Fig.1.6(c).

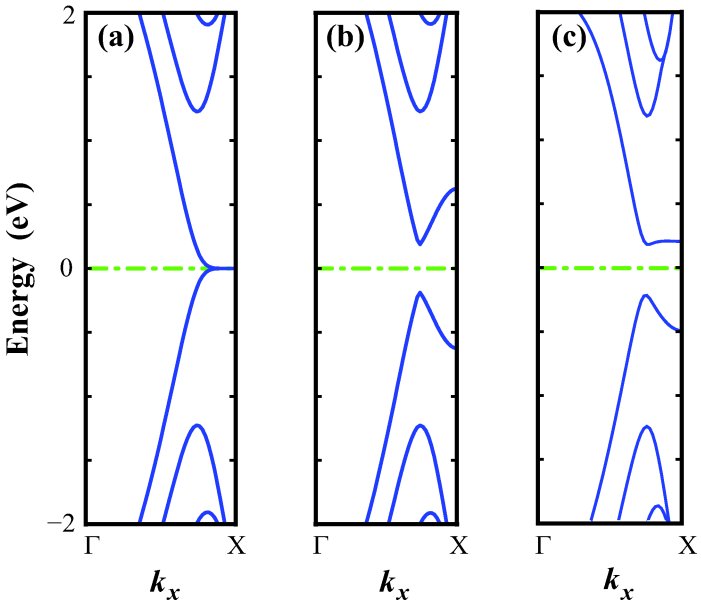

Figure 1.6: Band structures of ZGNR(8) calculated by using three different methods: (a) Tight-binding bands, (b) tight-binding bands including Hubbard correction within mean field approximation where $U = 1.3$ eV, and (c) bands obtained from plane-wave DFT calculations. Zero of the energy axis is set to E_F.

Chapter 2

Functionalization of Graphene and Graphene Nanoribbons

2.1 Electronic and Magnetic Properties of $3d$ Transition-Metal Atom Adsorbed Graphene and Graphene Nanoribbons

This section presents a detailed study of the magnetic and electronic properties of $3d$-transition metal (TM) adsorbed graphene and AGNRs using density functional theory. The equilibrium geometries, and electronic and magnetic properties are obtained using state-of-the-art *ab initio* total energy DFT calculations [see Appendix A]. We found that TM-atom decorated graphene shows different magnetic properties depending on the concentration and the species of TM-atoms. For single TM-atom adsorption to a unit cell of AGNR, the strongest binding occurs when the TM-atom is adsorbed above the center of the edge hexagon. In the case of two TM-atoms per unit cell, the second TM-atom prefers the hollow site of the neighboring hexagon so as to form a zigzag chain of TM-atoms at the edge of the AGNR. The magnetic properties of those species having strong binding are loosely affected by the ribbon width. Also, the adsorption of Fe and Ti to AGNR gives rise to half-metallic band structures.

2.1.1 Adsorption of Transition Metal Atoms on Graphene

Here, we investigate the electronic and magnetic properties of 2-dimensional graphene when Co, Cr, Fe, Mn or Ti atoms are adsorbed. We consider different coverages of TM-atoms, such as one TM-atom adsorbed on either (2×2) or (4×4) unit cells on only one side, as well as on both sides, namely, above and below the graphene. The geometrical configurations of the structures under consideration are represented in Fig. 2.1(a) and 2.1(b). Three different adsorption sites in the single-sided adsorption to (2×2) cell are considered. These consist of the hollow site (H1) being above the center of the hexagon, the bridge site (B1) over a C-C bond and the top site (T1) directly above a C atom (see Fig. 2.1(a)). For double-sided adsorption, when a TM-atom is adsorbed on H1-site from above, there are three more inequivalent possible sites B2, H2, and T2 as illustrated in Fig. 2.1(a).

First we discuss the results for the single-sided adsorption on the (2×2) cell. For all TM-atoms under consideration, binding to the H1-site is energetically more favorable except for Cr, which prefers the B1 site. In order to check the magnetic state of the structure, we double the previous geometry in both directions, and set the initial magnetic moments of TM-atoms to be antiferromagnetic (AFM).

In Table 2.1, we summarize the minimum energy geometries and the magnetic states of the single-sided adsorption on the (2×2) graphene cell, the corresponding binding energies and total magnetic moments of the systems. The total magnetic moments of the minimum energy states and the distance of the TM-atom to the nearest carbon atom are also included in Table 2.1. The binding energies are calculated as $E_b = E[\text{graphene}] + E[\text{TM}] - E[(\text{graphene+TM})]$ in terms of the total energies of the bare graphene per (2×2) cell, $E[\text{graphene}]$, the free TM-atom in its ground state $E[\text{TM}]$, and one TM atom adsorbed on a (2×2) cell of graphene, E[graphene]+E[TM]. All total energies are calculated in the same supercell keeping all the other parameters of the calculation fixed. The coupling between the TM-atoms, which is significant for the (2×2) cell calculations and hence weakens the TM-graphene binding, is subtracted from E_b. On the other hand, the TM-TM coupling is weaker in the case of a single atom

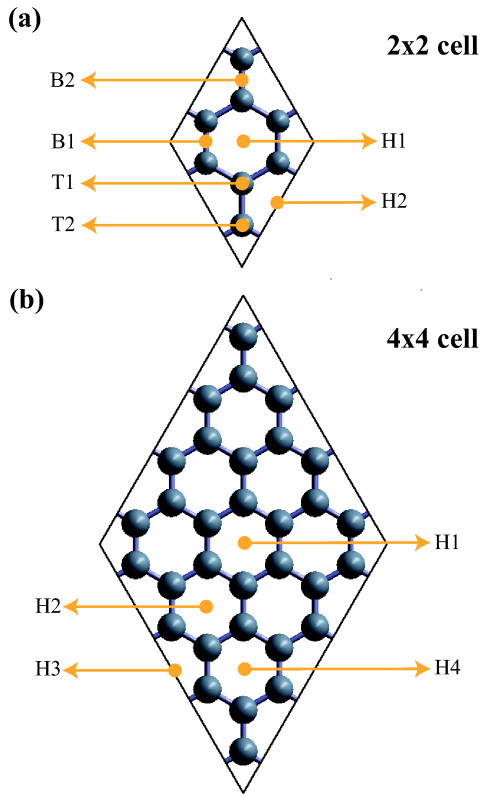

Figure 2.1: (a) A (2×2) cell of graphene and the six possible adsorption sites for the TM-atoms. B1, H1, and T1 are the single-sided adsorption sites, whereas B2, H2 and T2 are the possible additional sites for the double-sided adsorption. (b) A (4×4) cell of graphene and the four sites we consider for the adsorption of the second TM-atom from below when the first TM-atom is adsorbed on H1 from above. Calculations have been performed by using supercell geometry and hence the above adsorption geometries have been periodically repeated in two dimensions.

Table 2.1: Minimum energy adsorption sites and magnetic states (either ferromagnetic (FM) or antiferromagnetic(AFM)) for single-sided adsorption of one TM-atom adsorbed per (2×2) cell. The binding energies (E_b) ; the total magnetic moments μ_{tot} and the distances to the nearest C atom (d) are also listed. The binding energy of a single TM atom adsorbed on a (4×4) cell is given in parentheses for the sake of comparison.

	Ti	Co	Fe	Cr	Mn
	H1 AFM	H1 FM	H1 FM	B1 AFM	H1 AFM
E_b (eV)	1.58 (1.95)	1.20 (1.27)	0.66 (1.02)	0.18 (0.20)	0.10 (0.17)
μ_{tot} (μ_B)	0.0	1.31	3.02	0.0	0.00
d (Å)	2.32	2.12	2.21	2.39	2.47

adsorbed on the (4×4) cell; but the TM-graphene binding becomes stronger. Note that the decoration by TM atoms, where one TM-atom is adsorbed on each periodically repeating (4×4) cell of graphene can represent an isolated TM-atom adsorbed on graphene. We see that Cr and Mn do not have a considerable binding for any of the configurations. Their binding energies are 0.18 eV and 0.10 eV, respectively. Both Cr and Mn prefer AFM ground states. Binding energies of Ti, Co and Fe are relatively stronger and all prefer the H1-site. For Ti the minimum energy magnetic state is AFM, whereas for Co or Fe adsorbed graphene it is ferromagnetic (FM) with magnetic moments 1.31 μ_B (Bohr magneton) and 3.02 μ_B, respectively.

A few words about the states other than the minimum energy state is necessary to complete the discussion. First, the top site never yields a ground state for any of the TM atoms. No matter where the Co atom is initially placed (bridge, hollow or top site), it always finds its minimum energy state at the hollow H1 site after relaxation for both FM and AFM cases. On the other hand, Cr, Fe, Mn, and Ti which are initially placed at the T1 site within the FM state remain

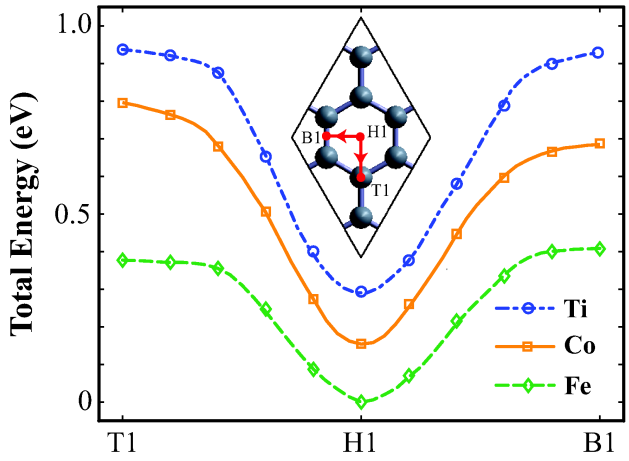

Figure 2.2: Analysis of the energetics of Ti, Co, and Fe moving from H1 to T1, and from H1 to B1. The transient paths are given in the inset. Total energy of the unit cell is plotted for each path (H1→T1, H1→B1) that are divided into sections with equal lengths.

at the T1 site upon the relaxation of the structure. Whereas Fe and Ti atoms, when they are placed at the T1 site in the AFM state, they drift to the H1 site and subsequently dimerize to occupy neighboring hexagons.

We further examined the energy of the system when the TM-atom is restricted to be adsorbed to the sites on the lines from H1 to T1, and from B1 to H1 for Co, Fe and Ti. During the relaxation of ionic positions, the $x-$ and $y-$ coordinates of the TM-atom are fixed, and the $z-$ coordinate is left free. Also the farthest C atom is fixed in the cell in order to ensure the relative position of the TM-atom with respect to the underlying graphene. In Fig. 2.2 the total energies of adsorption to the sites on the lines T1−H1 and H1−B1 are given. The energy minimum occurs at H1 whereas the energy barriers, ΔQ for adsorption to T1 are 0.38, 0.64, and 0.74 eV for Fe, Co, and Ti, respectively, and for adsorption to B1, ΔQ = 0.41, 0.53, and 0.74 eV, respectively. Accordingly, the diffusion of adsorbed Ti to form a cluster is prevented by significant potential barrier of 0.74 eV. However, the diffusion of Fe is relatively easy.

The band structures of the TM-atom adsorbed on the (2×2) graphene cell

Table 2.2: Minimum energy geometries and magnetic states for double-sided adsorption of two TM-atoms adsorbed per (2×2) cell. The binding energies (E_b), the total magnetic moments (μ_{tot}), and the distances of above (d) and below (d') TM-atoms to the nearest C atom are listed. The binding energies in parentheses correspond to the single-sided adsorption of one TM-atom on each (4×4) cell.

	Ti	Co	Fe	Cr	Mn
	H2 FM	H2 AFM	H2 AFM	B2 FM	H2 FM
E_b (eV)	1.79 (1.95)	1.11 (1.27)	0.60 (1.02)	0.33 (0.20)	0.26 (0.17)
μ_{tot} (μ_B)	0.14	0.0	0.0	0.16	9.77
d (Å)	2.28	2.18	2.24	2.41	2.46
d' (Å)	2.28	2.18	2.24	2.32	2.47

indicate that the systems are FM metallic for Co and Fe, AFM metallic for Ti, Cr, and Mn. We compare the band structures of the bare graphene folded according to the Brillouin zone of a (2×2) cell with that of one Co atom adsorbed on each (2×2) graphene cell (Fig. 2.3). As a result of Co adsorption new bands originating from Co cross the Fermi energy and the bands of underlying graphene are modified. Consequently the density of states at E_F increases, and the metalicity of graphene is enhanced.

In the double-sided adsorption, we tested six different sites for the second TM-atom keeping the first one at the H1-site. Considering FM and AFM configurations for the above and below TM-atoms we employed ionic relaxation. In Table 2.2 the minimum energy configurations and the binding energies for the adsorption of the second TM-atom, total magnetic moments of the structures and the distances of the TM-atoms to the nearest carbon atoms are listed. For Ti, Co, Fe, and Mn the energetically favorable adsorption site for the second TM-atom is the H2 site. The binding energies for the below Ti and Mn atoms are larger than

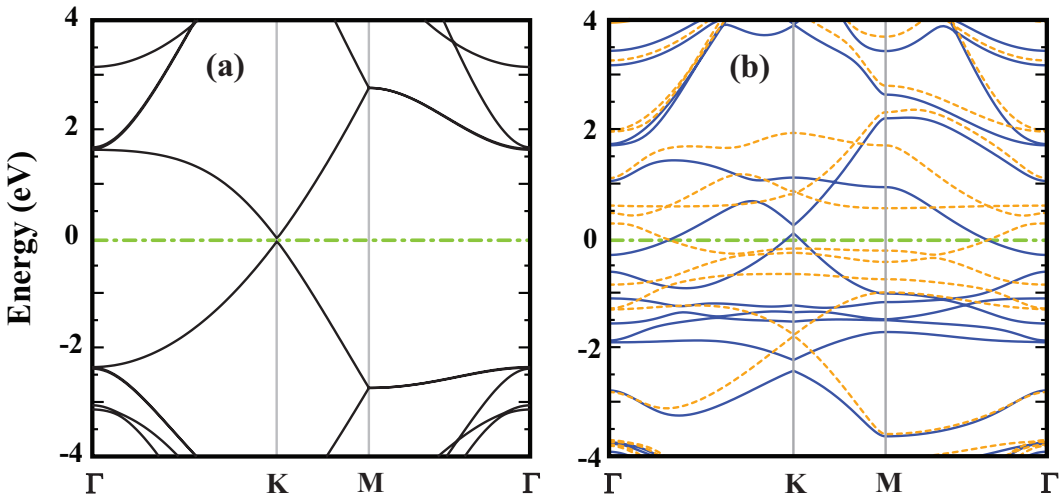

Figure 2.3: (a) Band structure of the bare graphene calculated for the (2×2) cell. (b) Band structure for one Co adsorbed to each (2 × 2) cell of graphene. Dark and light curves indicate the majority and minority spin bands respectively. The zero of the energy is set to the Fermi energy.

that of the single-sided adsorption, and their equilibrium positions are closer. On the contrary, for Co and Fe, the binding energies decrease and their distances to the C atoms increase. The analysis of the total magnetic moments indicates that for Co and Fe the above and below TM-atoms have opposite magnetic moments, but for Ti the net magnetic moment is finite but small. Mn atoms have parallel magnetic moments. Since not only the TM-graphene interaction but also the TM-TM interaction is effective in lowering the total energy of the system, one may expect the TM-atoms to prefer the adsorption site which enables the closest TM-TM distance possible. In double-sided adsorption, the smallest TM-TM distance is achieved by adsorption of both TM-atoms on the same hollow site from above and below. Our calculations show that such a configuration is not favorable energetically. Even tough the TM-TM interaction lowers the total energy, the TM-graphene interaction is also affected by the adsorption of both TM-atoms by the same carbon atoms. Consequently, the minimum energy states are those with TM-atoms adsorbed on H2 for Ti, Co, Fe, and Mn; and on B2 for Cr.

Table 2.3: Adsorption sites and corresponding magnetic states (FM or AFM), binding energies (E_b), total magnetic moments (μ_{tot}) and nearest carbon distances (d and d') for double-sided adsorption of one TM-atom adsorbed on each (4×4) cell from above and below. The first TM-atom is adsorbed on the H1 site from above.

	Ti	Co	Fe	Cr	Mn
	H2 AFM	H3 FM	H4 FM	H2 AFM	H3 FM
$E_{b,above}$ (eV)	1.95	1.27	1.02	0.18	0.17
$E_{b,below}$ (eV)	2.27	1.27	1.08	0.19	0.25
μ_{tot} (μ_B)	0.0	2.0	4.0	0.02	10.49
d (Å)	2.26	2.10	2.09	2.53	2.50
d' (Å)	2.26	2.10	2.08	2.55	2.53

We also investigate the double-sided adsorption of two TM-atoms on the (4×4) cell. We examined the adsorption of the second TM-atom on H2, H3, and H4 sites from below when the first is sitting above the H1 site (see Fig. 2.1(b)). The minimum energy configurations with binding energies and the total magnetic moments are given in Table 2.3. We note that the trade-off between the TM-TM interaction and the TM-graphene interaction in double-sided adsorption on a (2×2) cell holds also for the double-sided adsorption on a (4×4) cell.

The binding properties of TM-atoms on graphene are further analyzed by calculating the charge density difference of majority ($\uparrow$) and minority ($\downarrow$) spin states, i.e $\Delta\rho_{\uparrow(\downarrow)} = \rho_{\uparrow(\downarrow)}$[graphene+Ti] - $\rho_{\uparrow(\downarrow)}$[graphene] - $\rho_{\uparrow(\downarrow)}$[Ti] in the (4×4) unit cell. Here $\rho_{\uparrow(\downarrow)}$[graphene+Ti] is the total charge of the majority and minority spin states of one Ti atom adsorbed to each (4×4) cell of graphene. $\rho_{\uparrow(\downarrow)}$[graphene] and $\rho_{\uparrow\downarrow}$[Ti] are the charge densities of non-interacting bare graphene and Ti atom having the same positions as in the case of graphene and adsorbed Ti. All charge densities have been calculated in the same supercell. The plotted isosurfaces in

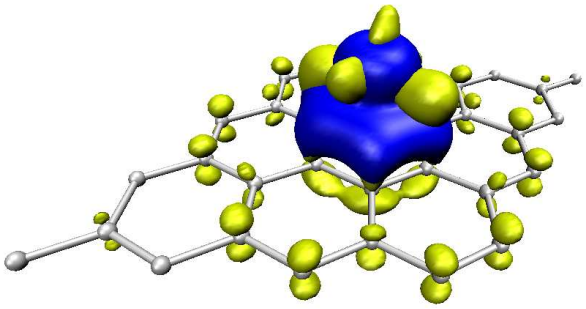

Figure 2.4: Spin resolved charge accumulation (i.e. $\Delta\rho_{\uparrow(\downarrow)} > 0$) obtained from the charge density difference calculation for one Ti atom adsorbed to each (4×4) cell of graphene (see the text). Dark and light regions indicate the isosurfaces of majority and minority spin states, respectively.

Fig. 2.4 show the accumulation in majority and minority spin charge densities as a result of the adsorption of Ti in comparison to noninteracting constituents. The isosurface plot shows an increase in majority spin density between graphene and Ti and a net increase in minority spin electrons on Ti. The difference in majority and minority spin densities demonstrates the induced magnetization on $2p_z$-orbitals of hexagon atoms.

2.1.2 Adsorption of Transition Metal Atoms on Graphene Nanoribbons

In this section, the spin dependent properties of TM-atom (Co, Cr, Fe, Mn, and Ti) adsorbed on AGNRs are presented. The variation of electronic and magnetic properties of AGNRs with different widths are examined. The dependence on the concentration of TM-atoms, and the effect of adsorption on different sites are studied in order to understand the variations and the origins of the magnetic properties. We define the TM-atom coverage θ as the number of TM-atoms per cell, and we study the cases with $\theta = 1$, and 2.

We first calculated the electronic structure of AGNRs with different widths and obtained consistent results with the earlier first-principles calculations [9].

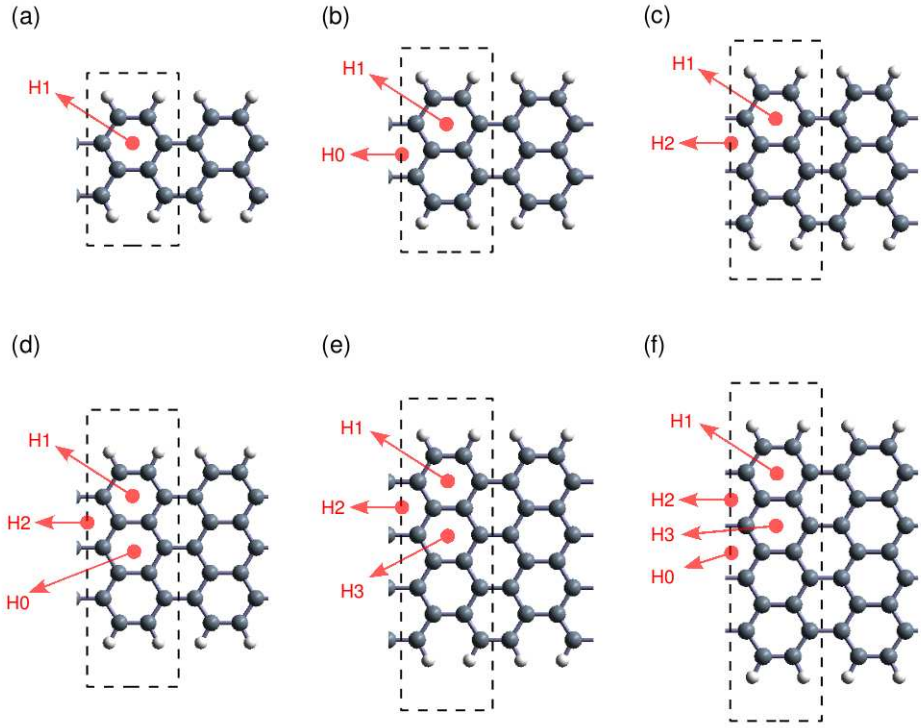

Figure 2.5: (a)-(f) possible hollow sites for adsorption to AGNRs with $N_a = 4$, 5, 6, 7, 8, and 9. For all N_a, H1 is the edge hollow site. H0 appears for $N_a = 5$, 7, and 9 which indicates that the middle hollow site fullfills the reflection symmetry. H2 and H3 are the remaining sites if they are different from the previous ones, H2 being closer to H1. The unitcells are indicated by dashed lines.

Table 2.4: Binding energies to possible sites of AGNR(N_a) shown in Fig. 2.5 (in units of eV).

		Ti	Co	Fe	Cr	Mn
AGNR(4)	H1	2.22	1.29	1.15	0.32	0.36
AGNR(5)	H0	2.16	1.12	0.97	0.38	0.25
	H1	2.29	1.37	1.14	0.52	0.43
AGNR(6)	H1	2.22	1.31	1.19	0.36	0.35
	H2	1.90	1.02	0.79	0.24	0.24
AGNR(7)	H0	1.84	0.90	0.72	0.23	0.03
	H1	2.24	1.29	1.17	0.38	0.35
	H2	2.02	1.06	0.91	0.24	0.08
AGNR(8)	H1	2.27	1.36	1.17	0.45	0.37
	H2	2.07	1.07	0.92	0.32	0.16
	H3	1.97	1.10	0.87	0.33	0.15
AGNR(9)	H0	1.99	1.08	0.94	0.25	0.07
	H1	2.24	1.32	1.18	0.38	0.35
	H2	1.95	1.05	0.84	0.26	0.06
	H3	1.90	1.02	0.79	0.25	0.01

Then we consider $\theta = 1$ coverage, where a single TM-atom is adsorbed per unit cell of AGNR. Due to the broken symmetry along the transverse direction, the number of possible adsorption sites increases with the width of the ribbon. We examined the hollow sites for the adsorption of all five species for AGNRs with $N_a = 4$, 5, 6, 7, 8, and 9. The adsorption sites under consideration are shown in Fig. 2.5. For all AGNRs considered, H1 is the hollow site at the very edge of the AGNR. H0 is the hollow site with equal distances to both edges, and exists for $N_a = 2n + 1$ only ($n \geq 2$). H2 and H3 are the remaining hollow sites which are not equivalent to H0 or H1, with H2 being closer to H1. The binding energies to these sites are given in Table 2.4.

For all TM species and for all AGNRs of different widths under consideration H1 is the energetically most favorable site for adsorption at $\theta = 1$. For $N_a = 7$, the second preferable site is H2 for all species. In $N_a = 9$ case, H0 becomes the second minimum energy adsorption site except for Cr, which prefers H2. When $N_a = 8$, H3 has less energy than H2 for Co and Cr whereas Mn and Ti have H2 as the second preferable adsorption site. Another difference between adsorption on AGNR and adsorption on graphene is that the TM-atoms stabilize their binding by gaining some displacement out of the center of the edge hexagon. This displacement has different values for different species, but as a rule of thumb, the stronger the binding, the smaller is the displacement.

Next, we analyze the transition state energies for AGNR(7) on the path from H0 to H1 over a bridge site as seen in Fig. 2.6(a) and (b). We choose equidistant 9 points along the path. During relaxation we fix the $y-$ and $z-$ coordinates of the closest carbon atoms forming the C-C bridge, and $x-$ and $y-$ coordinates of the Ti atom for each configuration leaving the rest of the coordinates free. The total energies of these configurations are plotted in Fig. 2.6(c). The energy barrier from H0 to H1 is $\Delta Q_{\mathrm{H0}\rightarrow\mathrm{H1}} = 0.48$ eV, while it is $\Delta Q_{\mathrm{H1}\rightarrow\mathrm{H0}} = 0.97$ eV in the reverse direction. These results suggest that the diffusion of adsorbed Ti atoms to form a cluster is hindered by the significant energy barrier ΔQ.

The magnetic states of H1-adsorbed AGNRs fall into two categories. Co and Ti adsorption produces FM metals for all widths of AGNRs, and Cr adsorption ends in AFM semiconductors with band gaps ranging between 0.07 eV to 0.56 eV depending on the ribbon width. (We note that the DFT method underestimates the band gaps found in these calculations[23]. However, this situation does not affect our conclusions in any essential manner.) On the other hand, Mn and Fe adsorptions do not exhibit that robust character. Mn adsorbed AGNR(6) is FM metal while for other N_a, Mn adsorbed AGNRs are AFM semiconductors with energy band gaps ranging between 0.40 and 0.69 eV. We observe that the species with strongest binding, i.e. Ti and Co, alter the semiconducting character of AGNRs to FM metals, while those with weakest binding (Cr and Mn) cannot metalize the ribbons and they generally prefer AFM alignment. For $N_a = 4$ and

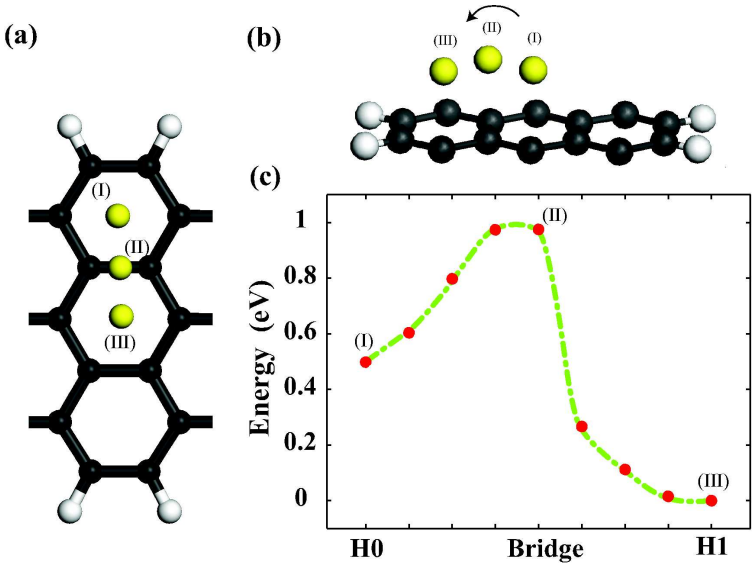

Figure 2.6: Transition state analysis of Ti adsorbed on AGNR(7) between H0 and H1 sites above the bridge site. (a) Top view of three adsorption sites of Ti on AGNR(7) from H0 to H1, i.e. H0, bridge and H1 sites are shown. (b) Side view for these three adsorption sites. Adsorption to the C-C bridge gives the farthest position to the AGNR plane. (c) Total energy per unit cell for Ti adsorption on the path from H0 to H1 (see the text).

$N_a = 7$, Fe adsorbed AGNRs are FM metals, for $N_a = 8$ it is half-metallic [24, 25] with an energy gap of 0.12 eV for minority spin, and AFM semiconductor for $N_a = 5$, $N_a = 6$, and $N_a = 9$. Half-metals are the materials which are relevant to spintronic applications due to their spin-dependent electronic properties. In these materials the spin degeneracy is not only broken but they are semiconductors foe one spin direction and they show metallic properties for the opposite spin direction. Accordingly the net spin in the unit cell is an integer and the spin polarization at the Fermi level (i.e. $P = |D_\uparrow(E_F) - D_\downarrow(E_F)|/(D_\uparrow(E_F) + D_\downarrow(E_F))$ in terms of the density of states at E_F for each spin state, namely $D_{\uparrow(\downarrow)}(E_F)$) is 100%. This situation is in contrast with the ferromagnetic metals where bands belonging to both spin directions contribute to the density of states at the Fermi level, and the spin polarization is less then 100%.

We also check the magnetic ground states of adsorption to H0 site of $\theta = 1$. H0 site is of special importance because its mirror symmetry in the transverse direction, and it exists only for $N_a = 2n + 1$ with $n \geq 2$. The TM-atom adsorbed on H0 site is at equal distance to the edges. Therefore one may expect the quantum interferences in this special geometry to have effects on the adsorption properties. Interestingly for Ti, Co, Fe and Cr the minimum energy states are always FM, and for Mn it is AFM.

For $\theta = 2$ adsorption, we consider one TM-atom to be adsorbed on the H1-site and the other on the H2-site which lowers the energy by TM-TM dimerization. We calculate three cases $N_a = 4$, 5, and 6 in order to sample the three families of AGNRs. For all cases the zigzag chains of TM-atoms at the edges either metalize the AGNRs or give rise to half-metalicity. We find that the zigzag chain of Fe on AGNR(5) is half-metallic with an energy gap of 0.10 eV for minority spin (Fig. 2.7(b)). Similarly, Ti zigzag chains on AGNR(4) and AGNR(5) are half-metallic with energy gaps of 0.05 eV and 0.16 eV, respectively for majority spin (Fig. 2.7(c)). Accordingly, TM-adsorbed AGNR is metallic for one spin-direction, but it is semiconductor for the opposite spin-direction. The calculated magnetic and electronic states of TM adsorbed AGNRs of $\theta = 1$ and 2 are summarized in Table 2.5. As seen the electronic structures and magnetic states show dramatic

Table 2.5: The magnetic ground states of TM-atom adsorbed AGNR(N_a) depending on TM coverage (θ) the width (N_a), and the adsorption site as described in Fig. 2.5. (AFM)FM-M(S): (antiferromagnetic) ferromagnetic-metal (semiconductor): HM:half-metal. Zigzag coverage for $\theta = 2$ refers to the zigzag chain of TM-atoms at the edge of the ribbon as explained in the text.

N_a	θ	site	Ti	Co	Fe	Cr	Mn
4	1	H1	FM-M	FM-M	FM-M	AFM-S	AFM-S
	2	zigzag	FM-HM	FM-M	FM-S	AFM-M	AFM-M
5	1	H1	FM-M	FM-S	AFM-S	AFM-M	AFM-M
	1	H0	FM-M	FM-M	FM-S	FM-M	AFM-M
	2	zigzag	FM-HM	FM-M	FM-HM	FM-M	FM-M
6	1	H1	FM-M	FM-M	AFM-S	AFM-S	FM-M
	2	zigzag	FM-M	FM-M	FM-M	FM-M	FM-M
7	1	H1	FM-M	FM-M	FM-M	AFM-S	AFM-S
	1	H0	FM-M	FM-M	FM-M	FM-M	AFM-M
8	1	H1	FM-M	FM-M	FM-HM	AFM-S	AFM-S
9	1	H1	FM-M	FM-M	AFM-S	AFM-M	FM-M
	1	H0	FM-M	FM-HM	FM-S	FM-M	AFM-M

variations depending on the adsorbate, the adsorption site, the adsorbate coverage (θ) and the width of the AGNR(N_a).

2.2 Confinement of Spin States in Graphene Nanoribbons

In this section, first-principles plane wave calculations[26] within density functional theory [21] (DFT) using projector augmented-wave (PAW) potentials[27] are performed [see Appendix A] to show that periodically repeated junctions of segments of zigzag ribbons with different widths can form stable superlattice

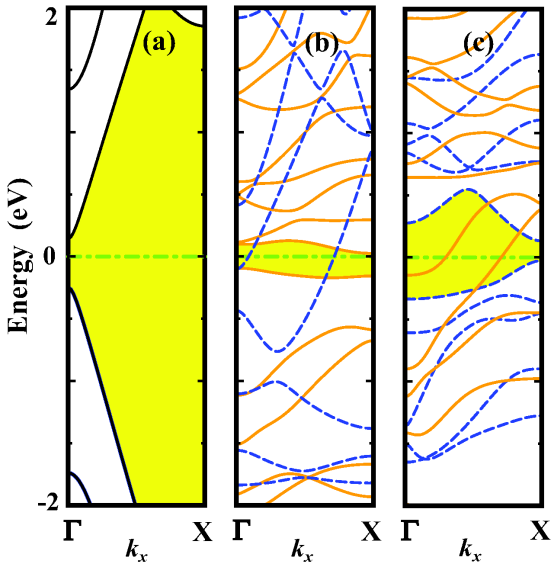

Figure 2.7: (a) Band structures of AGNR(5) and $\theta = 2$ coverages of AGNR(5) (b) with Fe, and (c) with Ti (c). Fermi Energy is set to zero. In (b) and (c), dark-dashed curves are the bands with majority spin, and light-solid curves are the bands of the minority spin. Fe adsorption opens a gap of 0.10 eV for the minority spin while the majority spin is metallic. Adsorption of Ti makes the minority spin metallic while the majority spin has an energy gap of 0.16 eV at the Fermi energy.

structures.

The energy band gap and magnetic state of the superlattice are modulated in the real space. Edge states with spin polarization can be confined in alternating quantum wells occurring in different segments of ribbons. Even more remarkable is that the antiferromagnetic (AFM) ground state can be changed to ferrimagnetic (FRM) one in asymmetric junctions.

Zigzag graphene ribbons, i.e. ZGNR(N_z) with N_z zigzag chains in its unit cell, are characterized by the states at both edges of ribbon with opposite spin polarization [16]. These edge states attribute an AFM character [see Section 1.2]. Under applied electric field the ribbon can become half-metallic [8]. Hydrogen saturated ZGNR(N_z) is an AFM semiconductor and has a band gap E_g, which decreases consistently for $N_z > 4$, and eventually diminishes as $N_z \to \infty$. In this section all zigzag ribbons are hydrogen terminated.

Let us now consider segments of two zigzag ribbons of different widths and different lengths, namely ZGNR(N_{z1}) and ZGNR(N_{z2}), which can make superlattice structures [28] with atomically perfect and periodically repeating junctions. Normally, the superlattice geometry can be generated by periodically carving small pieces from one or both edges of the nanoribbons [29]. Typical superlatices we considered and their structure parameters are schematically described in Fig. 2.8. ZGNR(N_{z1})/ZGNR(N_{z2}) superlattices can be viewed as if a thin slab with periodically modulated width in the xy-plane. The electronic potential in this slab is lower ($V < 0$) than outside vacuum ($V = 0$). Normally, states in this thin potential slab propagate along the $x-$axis; but the propagation of specific states in ZGNR(N_{z2}) is hindered by the potential barrier above and below the narrow segment, ZGNR(N_{z1}). Eventually, these states are confined to the wide segments, and in certain cases also to the narrow segments. Here the confinement of the states has occurred due to the geometry of the system. Defining the confinement in a segment i as $\int_i |\Psi(\mathbf{r})|^2 d\mathbf{r}$, the sharper the interface between ZGNR(N_{z1}) and ZGNR(N_{z2}) the stronger becomes the confinement.

In Fig. 2.9, we show a symmetric superlattice ZGNR(4)/ZGNR(8). Spin-up and spin-down edge states at the top of the valence band of AFM superlattice are

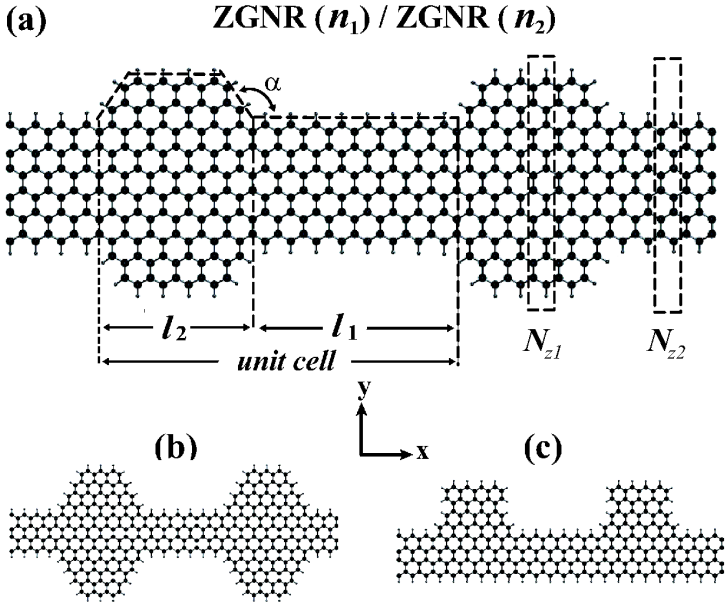

Figure 2.8: Typical superlattice structures of zigzag graphene ribbons, ZGNR(N_{z1})/ZGNR(N_{z2}). N_{z1} and N_{z2} are the number of zigzag chains in the longitudinal direction; l_1 and l_2 are lengths of alternating ZGNR segments in numbers of hexagons along the superlattice axis. α is the angle between the $x-$axis and the edge of the intermediate region joining ZGNR(N_{z1}) to ZGNR(N_{z2}). $\alpha = 120^o$ for (a) and (b); 90^o for (c). Dark-large balls and small-light balls indicate carbon and hydrogen atoms, respectively.

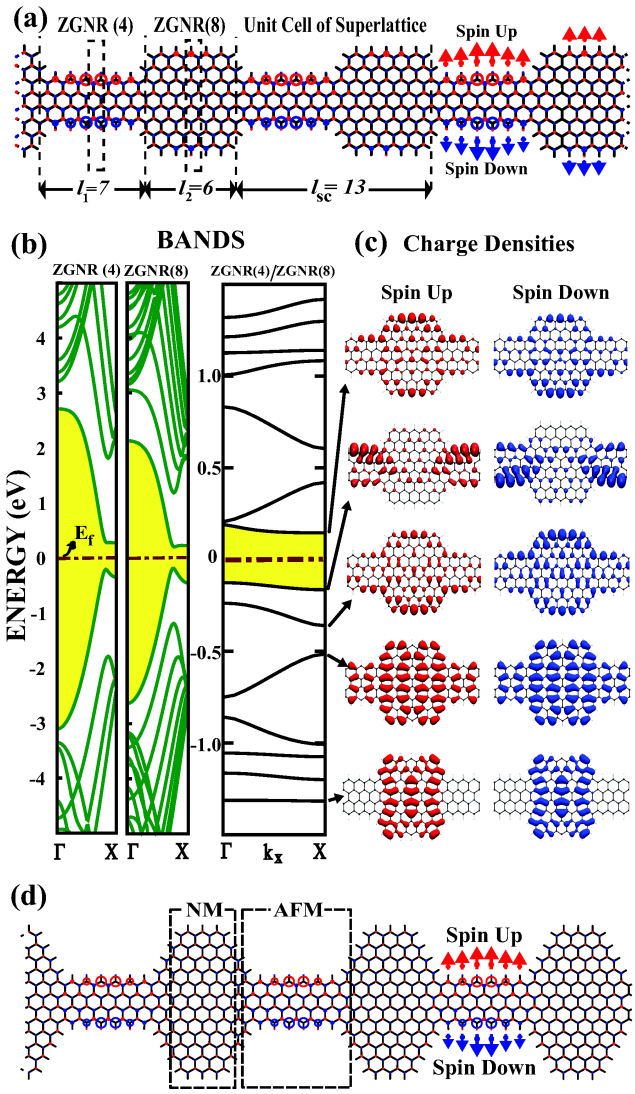

Figure 2.9: (a) A schematic description of the symmetric ZGNR(4)/ZGNR(8) superlattice with relevant structural parameters. Magnetic moments on the atoms are shown in the left cell by dark and light circles and arrows for positive and negative values. l_{sc} is the length of the superlattice unitcells in terms of number of hexagons along the $x-$axis. (b) Energy band structures of antiferromagnetic (AFM) ZGNR(4), ZGNR(8) ribbons and AFM ZGNR(4)/ZGNR(8) superlattice. (c) Charge density isosurfaces of specific superlattice states. Zero of the energy is set to Fermi level, E_F. The gap between conduction and valence bands are shaded. (d) A specific form of superlattice ZGNR(4)/ZGNR(12) with alternating AFM and nonmagnetic (NM) segments in real space.

confined to the opposite edges of the narrow segments of the superlattice. Normal flat band states near -1.2 eV are confined to the wide segments of ZGNR(8). The energy band structure of the superlattice is dramatically different from those of the constituent nanoribbons. If the lengths of the segments are sufficiently large, these segments display the band gap of the corresponding infinite nanoribbon in real space. The total magnetic moment of spin-up and spin-down edge states is zero in each segment, but the magnetic moment due to each edge state is different in adjacent segments. As a result, the superlattice is remained to be AFM semiconductor, but the magnitudes of the magnetic moments of the edge states are modulated along the $x-$axis. The coupling between the magnetic moments localized in the neighboring segments is calculated to be 15 meV per unit cell. The modulation of magnetic moments can be controlled by the geometry of the superlattice. For example, as shown in Fig. 2.9(d), the magnetic moments of the atoms in the wide segment are practically zero and hence the superlattice is composed of AFM and nonmagnetic (NM) segments. However, as $l_2 \rightarrow 10$ the magnetic moments of the edge atoms at the wide segment become significant.

The situation is even more interesting for an asymmetric superlattice as shown in Fig. 2.10. While the spin-down states remain propagating at the flat edge of the superlattice, spin-up states are confined predominantly at the opposite edge of the wide segments. Confinement of states and absence of reflection symmetry breaks the symmetry between spin-up and spin-down edge states. Hence superlattice formation ends up with a FRM semiconductor having different band gaps for different spin states. In agreement with Lieb's theorem [22, 30], the net magnetic moment calculated to be 2 μ_B is equal to the difference of the number of atoms belonging to different sublattices. Flat bands at the edges of spin-up valence band and spin-down conduction band are of particular interest. The spin-states of these bands are confined at the discontinuous edges of the wide segment which behave as a quantum well. Since a device consisting of a finite size superlatice connected to two electrodes from both ends has high conductance for one spin direction, but low conductance for the opposite one, it operates as a spin-valve. Moreover, spin-down electrons injected to this device are trapped in one of the

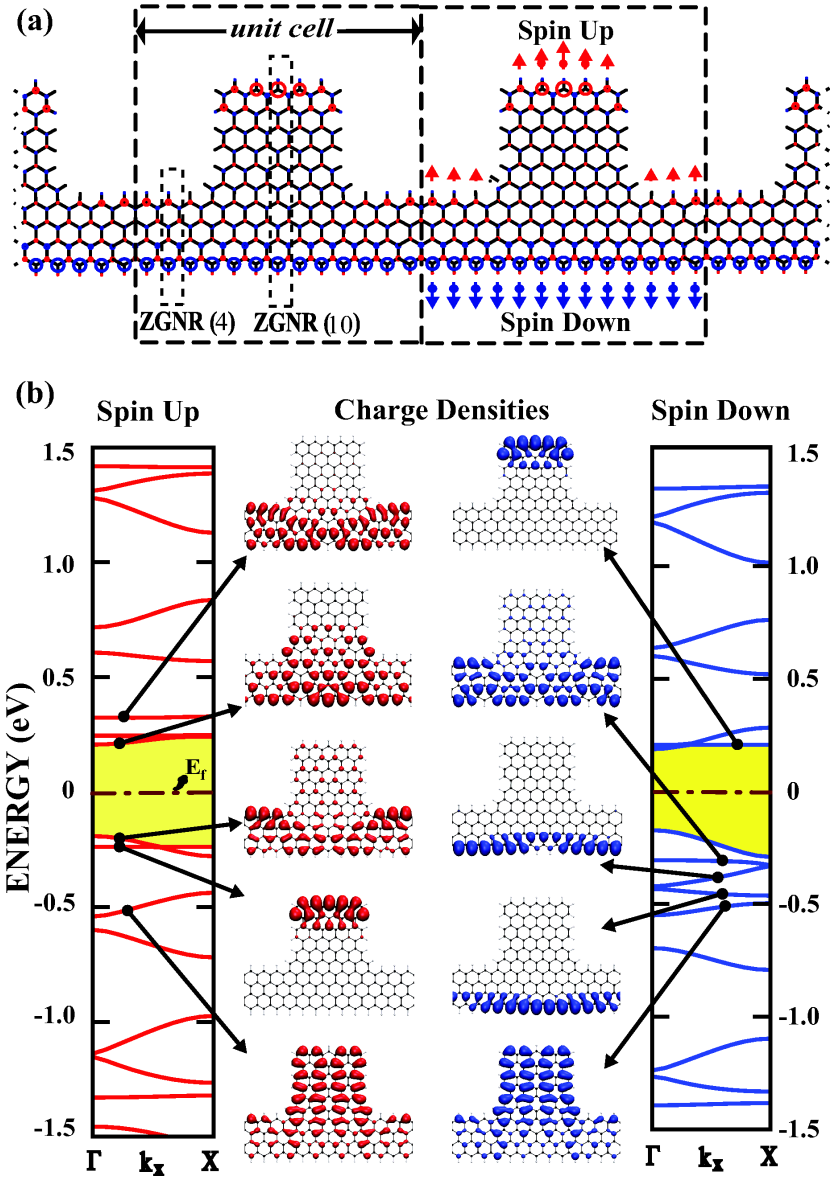

Figure 2.10: (a) A schematic description of an asymmetric ZGNR(4)/ZGNR(10) superlattice. Total majority and minority spins shown by light and dark circles (for spin-up and spin-down, respectively) attribute a ferrimagnetic (FRM) behavior. (b) Energy band structure of the FRM semiconductor and charge density isosurfaces of specific propagating and confined states of different spin-polarization.

quantum wells generated in a wide segment. As a final remark, we note that the DFT method underestimates the band gaps found in this work[23]. However, this situation does not affect our conclusions in any essential manner.

2.3 Graphene Based Resonant Tunneling Double Barrier Device

In this section, we focus on a finite segment of graphene nanoribbon and calculate its transport properties. In accordance with the results of the previous section, we investigate the effect of confinement on transport properties upon modulation of the ribbon width. We consider a finite armchair graphene nanoribbon with AGNR(5) and AGNR(9) as constituent parts having total length of 8 unitcells as shown in Fig. 2.11. Such a device is relevant for applications and uses highest occupied (HOMO) and lowest unoccupied molecular orbitals (LUMO) confined in the wide region.

Patterning of graphene nanoribbons [31], and also graphene nanoribbons with varying widths [32, 33] are achieved, and it is shown experimentally that transport through graphene nanoribbons is primarily influenced by the boundary shape [31]. These experiments reveal the importance of charge confinement effects on the conductance. Moreover, a suppression of conductance of graphene nanoribbons by Coulomb blockade due to formation of multiple quantum dots in series which are likely to form during the etching process is also reported[33]. These facts support our idea that construction of a double barrier device by modulating the width of a nanoribbon is realizable experimentally.

The electronic transport calculations are carried out using two different approaches: The Landauer approach using Green's functions [34, 35], and the Keldysh approach using density functional theory. Below we summarize the first approach, details of the second approach can be found in Ref. [36].

In the transport calculations a fictitious partitioning scheme is employed in which the system is defined with the free Hamiltonians for the left and right

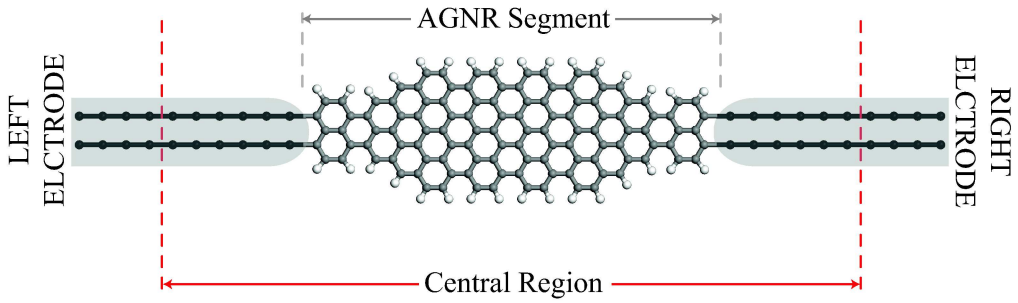

Figure 2.11: Resonant tunneling double barrier device consisting of AGNR(5) and AGNR(9) segments. Parts of electrodes are included at both sides of AGNR segment as parts of the central device.

semi-infinite electrodes, and for the central region; and the coupling Hamiltonians between the electrodes and the central region as illustrated in Fig. 2.11. In order to be able to apply such a partitioning scheme we use localized orbitals which, in general, do not define an orthogonal basis set. The total Hamiltonian and the corresponding overlap integrals can be written in matrix form as

$$\mathbf{H} = \begin{pmatrix} H_L & \tau_{LC} & 0 \\ \tau_{LC}^{\dagger} & H_C & \tau_{RC}^{\dagger} \\ 0 & \tau_{RC} & H_R \end{pmatrix} \qquad \mathbf{S} = \begin{pmatrix} S_L & S_{LC} & 0 \\ S_{LC}^{\dagger} & S_C & S_{RC}^{\dagger} \\ 0 & S_{RC} & S_R \end{pmatrix} \tag{2.1}$$

where the subscripts $L(R, C)$ stand for the left electrode (right electrode, central region), and the off-diagonal terms stand for the couplings between the parts. The retarded Green's function is defined through the matrix multiplication $[\epsilon\mathbf{S} - \mathbf{H}]\mathbf{G} = \mathbb{1}$ where $\epsilon = (E + i0^{+})$, E being the energy variable, $\mathbb{1}$ is the identity matrix and $\mathbf{G}$ is also partitioned as

$$\mathbf{G} = \begin{pmatrix} G_L & G_{LC} & G_{LR} \\ G_{CL} & G_C & G_{CR} \\ G_{RL} & G_{RC} & G_R \end{pmatrix}. \tag{2.2}$$

Performing the matrix multiplication for the second column of $\mathbf{G}$ only, one arrives at the following relations

$$(\epsilon S_L - H_L)G_{LC} + (\epsilon S_{LC} - \tau LC)G_C = 0, \tag{2.3}$$

$$(\epsilon S_{LC}^{\dagger} - \tau_{LC}^{\dagger})G_{LC} + (\epsilon S_C - H_C)G_C + (\epsilon S_{RC}^{\dagger} - \tau_{RC}^{\dagger})G_{RC} = \mathbb{1}, \quad (2.4)$$

$$(\epsilon S_{RC} - \tau_{RC})G_C + (\epsilon S_R - H_R)G_{RC} = 0. \quad (2.5)$$

The off-diagonal terms of the Green's function appearing in the above relations can be written in terms of G_C and the free Green's functions using Eqn. 2.3 and Eqn.2.5 as

$$G_{LC} = -g_L(\epsilon S_{LC} - \tau_{LC})G_C, \quad (2.6)$$

$$G_{RC} = -g_R(\epsilon S_{RC} - \tau_{RC})G_C, \quad (2.7)$$

where g_L and g_R are the free Green's functions for the semi-infinite electrodes (For an iterative calculation of the free electrode Green's functions see Appendix B). Hence the Green's function of the central region is obtained as

$$G_C = \left[(\epsilon S_C - H_C) - \Sigma_L - \Sigma_R\right]^{-1}, \quad (2.8)$$

$\Sigma_{L(R)}$ being the self-energies due to coupling to the left (right) electrodes,

$$\Sigma_{L(R)} = \left[\epsilon S_{LC(RC)}^{\dagger} - \tau_{LC(RC)}^{\dagger}\right] g_{L(R)} \left[\epsilon S_{LC(RC)} - \tau_{LC(RC)}\right]. \quad (2.9)$$

Having obtained the coupled Green's function for the central region in terms of the free Green's functions of the constituent parts, we can calculate the energy dependent transmission coefficient by Fischer-Lee formula [37] as

$$T = \mathrm{Tr}\left[\Gamma_L G_C \Gamma_R G_C^{\dagger}\right], \quad (2.10)$$

where $\Gamma_{L(R)}$ stand for the level broadenings due to couplings to the left (right) electrodes, and they are defined as $\Gamma_{L(R)} = -2\,\mathrm{Im}\left[\Sigma_{L(R)}\right]$.

In the calculations of the RTDB device, we considered generic metallic electrodes of two widely separated (weakly coupled) monatomic carbon chains. Carbon chains are known to have high cohesive energy and axial strength, and exhibit stability even at high temperatures [38]. Because of their flexibility and reactivity, carbon chains are suitable for structural and chemical functionalizations, and they are good metals with 2 quantum conductance channels which make 4 units of quantum conductance at the Fermi level for

the electrodes we consider. Six principal layers of electrodes are included at both sides of RTDB as parts of the central device. Metallic electrodes make perfect contacts with the central RTDB device. The Hamiltonans for the electrodes and the central region are written using the tight-binding parametrization of Section 1.1. That is, we use the empirical tight-binding parameters of Ref. [14] in which a single-level parametrization is employed where the on-site energy is taken as zero and the nearest neighboor hopping term is $t = 2.7$ eV. Once the geometrical structure is determined, the Hamiltonians are generated and the energy levels are calculated with a computer code developed by the author. Using the Hamiltonians H_L, H_R, H_C, τ_{LC} and τ_{RC}, the transmission spectrum of the central region is calculated by another computational code developed by the author which implements the method summarized above and the surface Green's function matching technique presented in Appendix B. The transmission coefficient T reflects the combined electronic structure of central RTDB device, electrodes and their contacts as shown in Fig.2.12(a) (solid curves).

The confined lowest occupied and highest unoccupied molecular states and other confined states are identified through the energy level diagram [see Fig. 2.12(b)] and isosurface charge density plots obtained from plane wave *ab-initio* calculations [see Fig. 2.12(c)]. The confined states give rise to sharp peaks originating from resonant tunneling effect. States extending to whole RTDB are coupled with the states of electrodes and they are shifted and contributed broader structures in the transmission curve. Calculations using the Keldysh approach within density functional theory yield very similar results as can be seen in Fig. 2.12(a) and (b) (dashed curves). In these calculations double-ζ plus polarization numerical orbitals have been used as the basis set, and the atomic structures are further optimized before transport calculations. Even tough it is possible to obtain more accurate results using the Landauer approach by extracting the Hamiltonians from local orbital DFT calculations, the empirical tight-binding based calculations yield results which are in good agreement both qualitatively and quantitatively with the *ab-initio* non-equilibrium code, ATK [36]. One should note that, since a single level approach is used in our empirical

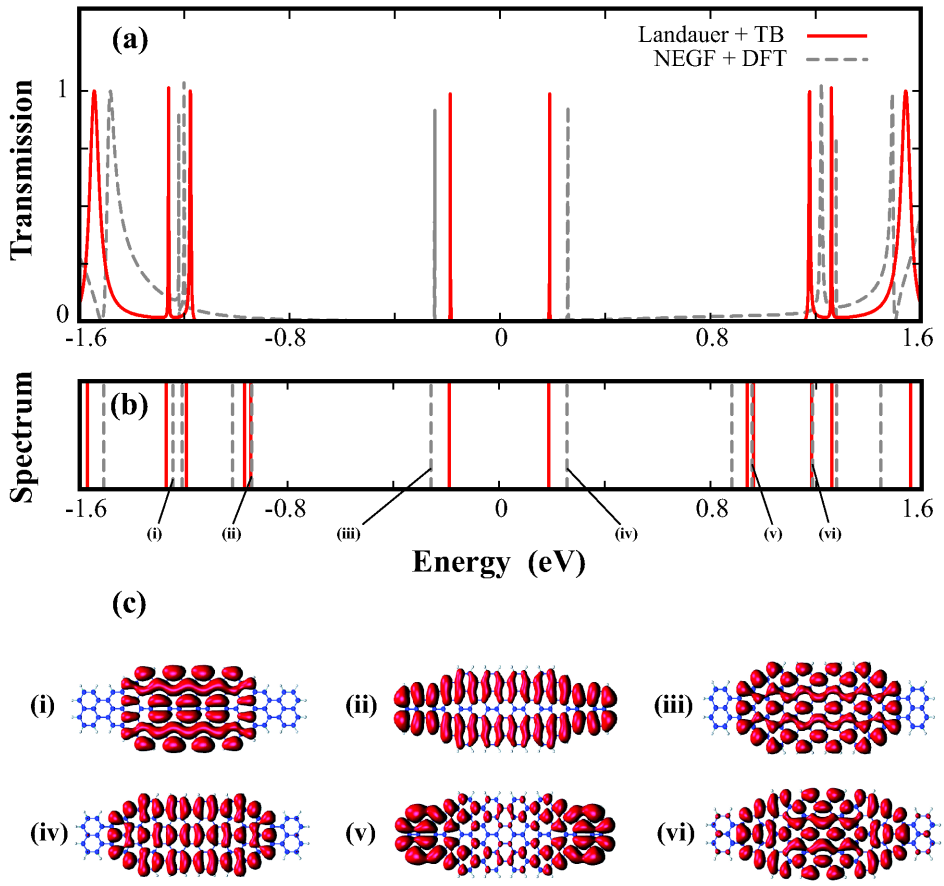

Figure 2.12: (a) Transmission coefficient T versus energy calculated under zero bias. Zero of the energy axis is set to the Fermi level. (b) The energy spectrum of the uncoupled AGNR segment. (c) Charge densities of selected energy levels of the uncoupled AGNR segment indicating confined versus extended states.

tight-binding based transport calculations, those levels originating from sp^2 hybridization of carbon atoms do not contribute to the results whereas these levels are taken into account properly in our calculations using the Keldysh approach. Evidently, comparing the molecular spectrum (Fig. 2.12(b)) and the transmission coefficients (Fig. 2.12(a))obtained by both methods, it can be observed that these levels are lying out of the energy window we consider.

Chapter 3

Phononic Dissipation at the Atomic Scale

Friction between two surfaces in relative motion involves many interesting and complex phenomena induced by the long- and short-range forces, such as adhesion, wetting, atom exchange, bond breaking and bond formation, elastic and plastic deformation[39–52]. In general, non-equilibrium phonons are generated in the expense of damped mechanical energy [53–58]. Dissipation of this excess energy is one of the important issues in dry-sliding friction and lubrication [48, 59–61]. Normally, the dissipation of mechanical energy is resulted in heating of parts in relative motion. Sometimes, it gives rise to wear and failure due to overheating. In general, significant amounts of resources (energy and material) are lost in the course of friction. One of the prime goals of tribology is to minimize energy dissipation through lubrication. Recently, several works have attempted to develop surfaces with superlow friction coefficients [62].

In the past, the energy dissipation during sliding has been usually investigated in the macroscopic scale by using simple Tomlinson's model [41]. Hence, the dissipated energy and friction force has been revealed indirectly from stick-slip motion. The objective of this study is to develop a microscopic (or atomic scale) understanding of phononic energy dissipation during sliding friction, especially

to shed some light on the dynamics of discharge of excited phonons on a nano-particle (representing a lubricant molecule or an asperity) into the substrate. This problem has many aspects and the solution will depend on a variety of physical parameters which can be grouped into major categories, such as internal degrees of freedom of the nano-particle, density of substrate phonon modes, the type and strength of coupling between the nano-particle and the substrate, and finally the initial temperatures. One way of studying this problem could be carrying out state-of-the-art molecular dynamics simulations which yields sample specific results only. However, to explore the general features of the phononic dissipation, we propose an Hamiltonian treatment of the problem. Since the number of physical ingredients determining the dynamics is considerably large, our strategy will be to focus on them separately to reveal their role in energy dissipation.

In this chapter, we present our analysis concerning the dependence of phononic dissipation on internal degrees of freedom of the nano-particle and the substrate by using two types of coupling between the finite and extended systems. We consider three different theoretical methods; namely the equation of motion (EoM) technique which involves Laplace transforms for the solution of the coupled differential equations for phonon operators, the Fano-Anderson (FA) method which is useful for diagonalizing quadratic Hamiltonians, and Green's Function (GF) method by which we can incorporate the effect of multi-modes into the study. The first two methods have limited applicability for specific cases only, and will be presented for completeness. The GF method, being the most general method, will be extensively discussed. We also note that, the GF method allows solutions beyond linear response where the EoM and FA methods yields solutions within the linear response regime [63].

The organization of this chapter is as follows. In Section 3.1, we describe the physical model. The theoretical methods to be used and their limitations are presented in Section 3.2. The applications of theoretical methods to different types of coupling and substrates having different densities of states will be presented and discussed in Section 3.3. These are mainly the dependence of the

decay rate on the coupling constant, the interaction-specific dependence of decay rate on the nano-particle mode frequencies and the effect of neighboring modes on decay rate of each other. Finally, we present a specific and realistic example, where the dissipation of vibrational modes of benzene molecule (C_6H_6) to a graphene substrate is analyzed by using density functional theory calculations.

3.1 The Model

We first consider a nano-particle representing a lubricant molecule or an asperity, which is weakly coupled to a substrate (Fig. 3.1). The vibrational modes of the nano-particle are excited initially and the excess phonons discharge to the bulk. The total Hamiltonian of the system can be written as

$$H = H_M + H_S + H_{MS} \tag{3.1}$$

where H_M, H_S are the free phononic Hamiltonians of the nano-particle (or molecule) and the substrate (or bath), respectively; the interaction between them is represented by H_{MS}. We also define $H = H_0 + H_{MS}$. We assume that the harmonic approximation is good enough for H_M and H_S, and their phonon spectra are known, i.e.

$$H_M = \sum_j \hbar\omega_j \, a_j^+ a_j, \tag{3.2}$$

$$H_S = \sum_{\mathbf{k}} \hbar\omega_{\mathbf{k}} b_{\mathbf{k}}^+ b_{\mathbf{k}}. \tag{3.3}$$

Here, ω_j are the frequencies of the nano-particle modes with a_j, a_j^+ being the corresponding annihilation, creation operators; $\omega_{\mathbf{k}}$ are frequencies of the substrate vibration modes of wavevectors $\mathbf{k}$, and $b_{\mathbf{k}}$, $b_{\mathbf{k}}^+$ are the corresponding phonon annihilation, creation operators. We have omitted the constant terms as they do not contribute to the dynamics of the system. Here we consider a single phonon branch without loosing generality, but the formalism can be extended to include multiple branches. The interaction Hamiltonian H_{MS} is also assumed to

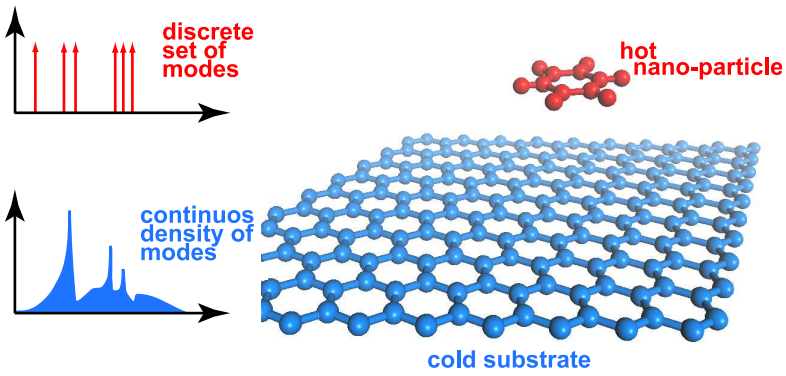

Figure 3.1: A nano-particle with discrete density of phonon modes is coupled to a substrate having continuous density of modes.

be quadratic in phonon operators,

$$H_{MS} = \sum_{\mathbf{k},j} \hbar \left(W_{\mathbf{k}j} b_{\mathbf{k}}^{+} a_j + h.c. \right) \tag{3.4}$$

with $W_{\mathbf{k}j}$ being the coupling coefficient which is a function of $\omega_{\mathbf{k}}$ and ω_j, and has the dimension of angular frequency. We disregard the double annihilation and double creation of phonons in the present work.

Here we consider two types of coupling. The first one is Lorentzian coupling in which the coupling coefficient $W_{\mathbf{k}j}$ is a Lorentzian with its peak located at ω_j and has width Γ_j. As long as the coupling between the nano-particle and the substrate is weak, $W_{\mathbf{k}j}$ will be a peaked function of $\omega_{\mathbf{k}}$ and a separate peak will be present around each ω_j. Depending on the strength of the interaction, the sharpness of the peaks and the overlap between the neighboring peaks will differ. If the coupling is weak enough we may neglect the overlaps, namely

$$W_{\mathbf{k}l}^{*} W_{\mathbf{k}j} \rightarrow |W_{\mathbf{k}l}|^2 \delta_{l,j}. \tag{3.5}$$

For Lorentzian coupling, we assume that the coupling terms of different modes of the nano-particle do not overlap, and hence we can treat each nano-particle mode separately.

For the second type of coupling, we consider the coupling coefficients which scale inversely as the square root of the product of the frequencies of the coupled modes, i.e.

$$W_{\mathbf{k}j} = \alpha \left(\omega_{\mathbf{k}}\omega_j\right)^{-1/2}. \tag{3.6}$$

The coefficient α stands for the strength of the coupling and will depend on the interaction between the nano-particle and the substrate. In both coupling types, $W_{\mathbf{k}j}$ is a function of $\omega_{\mathbf{k}}$ and ω_j, explicit dependence on the wavevectors is not included for the sake of simplicity. In this study, we consider the initial temperatures to be zero and limit our attention to the near-equilibrium case in the weak coupling regime. The effect of initial temperatures of the parties, besides from the effect of temperature difference, is another major topic in its own and we refer the reader to the note in Appendix E for the non-equilibrium formulation of the problem.

3.2 Theoretical Methods

3.2.1 Equation of Motion (EoM) Technique

The time dependent occupancies of the nano-particle modes can be obtained using Heisenberg's equation of motion, namely $\dot{A}(t) = i[H, A(t)]/\hbar$. The equations of motion for the phonon annihilation operators are

$$\dot{a}_l(t) = -i\omega_l a_l(t) - i\sum_{\mathbf{k}} W^*_{\mathbf{k}l} b_{\mathbf{k}}(t), \tag{3.7}$$

$$\dot{b}_{\mathbf{k}}(t) = -i\omega_{\mathbf{k}} b_{\mathbf{k}}(t) - i\sum_{j} W_{\mathbf{k}j} a_j(t), \tag{3.8}$$

that is we have coupled differential equations for each operator. As the solution procedure is outlined in Ref. [64], by performing Laplace Transformation to both equations, a pair of coupled algebraic equations is obtained which can be decoupled algebraically, and by inverse transformation the time dependent

operator $a_l(t)$ is obtained as

$$a_l(t) = \frac{a_l(0)}{2\pi i} \oint_B \frac{e^{st} ds}{s + i\omega_l + I_l(s)} - \frac{1}{2\pi} \oint_B \frac{e^{st} J_l(s) ds}{s + i\omega_l + I_l(s)}. \tag{3.9}$$

where the integrals are to be evaluated along the Bromwich contour, with $I_l(s)$ and $J_l(s)$ being substrate and interaction specific functions (see Appendix C).

The first and second terms in Eq. (3.9) stand for contributions from the initial excitation of the nano-particle and the initial temperature of the substrate respectively. The second term does not contribute to the time dependent occupations of the nano-particle mode, since the initial temperature of the substrate is considered to be zero.

3.2.2 Fano-Anderson (FA) Method

Since the Hamiltonian is quadratic in operators, its solution is equivalent to diagonalizing a matrix. Exact diagonalization of such quadratic Hamiltonians was shown to be possible by Fano[65] and Anderson [66] independently and the procedure is widely used in atomic physics, solid state physics, quantum optics, etc. Here, we will apply their method to the problem of phononic dissipation.

Solution of the Hamiltonian is equivalent to finding the dressed operators $\alpha(\omega_{\mathbf{q}})$ such that the Hamiltonian is diagonal in terms of the dressed operators, $H = \sum_{\mathbf{q}} \hbar\omega_{\mathbf{q}}\, \alpha^+(\omega_{\mathbf{q}})\alpha(\omega_{\mathbf{q}})$.

As described in Appendix D, one can write the time dependent occupancy of j^{th} mode as

$$\begin{aligned} \langle n_j(t)\rangle = \langle n_j(0)\rangle \left| \int d\omega_{\mathbf{q}}\, g(\omega_{\mathbf{q}})\, |\mu(\omega_{\mathbf{q}}, \omega_j)|^2 e^{-i\omega_{\mathbf{q}} t} \right|^2 \\ + \int d\omega_{\mathbf{k}} g(\omega_{\mathbf{k}}) \langle n_{\mathbf{k}}(0)\rangle \left| \int d\omega_{\mathbf{q}}\, g(\omega_{\mathbf{q}})\, \mu^*(\omega_{\mathbf{q}}, \omega_j)\, \nu^*(\omega_{\mathbf{q}}, \omega_{\mathbf{k}}) e^{-i\omega_{\mathbf{q}} t} \right|^2 \end{aligned} \tag{3.10}$$

where $\mu(\omega_{\mathbf{q}}, \omega_j)$ are the expansion coefficients for the molecular operator a_j in terms of the dressed operators $\alpha(\omega_{\mathbf{q}})$; and $\nu(\omega_{\mathbf{q}}, \omega_{\mathbf{k}})$ are that of the substrate operator $b_{\mathbf{k}}$ (see Appendix D).

Due to the finite range of substrate DOS $g(\omega_{\mathbf{k}})$, the integrals involved in the FA Method are bounded, the method allows us to perform calculations for any $g(\omega_{\mathbf{k}})$ and for any type of coupling with a single nano-particle mode. The time dependent occupation is again separable as contributions from the initial temperature of the nano-particle and that of the substrate. However, it should be noted that, the FA Method is applicable for any coupling type and any density of states for the substrate as long as we consider a single nano-particle mode.

3.2.3 Green's Function (GF) Method

The effect of neighboring modes of nano-particle having multi-modes cannot be resolved within the above methods. That is, EoM and FA methods are restricted to the linear response regime. We use a more generalized method by which one can consider effects of neighboring modes. For this purpose we employ Green's Functions. (For a review of Green's function method in many-particle physics see Ref. [67].) Initially the substrate temperature is zero and the phonon modes of the nano-particle are empty except for the excitations which do not necessarily obey Bose-Einstein distribution. That is the initial occupation of a nano-particle mode is not a function of temperature. Therefore we make use of zero temperature Green's Functions instead of Matsubara formalism,

$$d(j,t-t') = -i\langle T_t \hat{a}_j(t)\hat{a}_j^+(t')\rangle \tag{3.11}$$

$$D(\mathbf{k},t-t') = -i\langle T_t \hat{b}_{\mathbf{k}}(t)\hat{b}_{\mathbf{k}}^+(t')\rangle \tag{3.12}$$

where T_t is the time-ordering operator, and the operators in Heisenberg picture are distinguished by a hat. Here we should note that such definitions for phonon Green's functions are not widely used in literature, but considering our model Hamiltonian these definitions are more appropriate.

Since each term in the interaction Hamiltonian includes odd number of nano-particle operators, only the even order terms contribute in the expansion. The first contribution due to the interaction is the second order term,

$$d^{(0)}(\omega_j)^2 \sum_{\mathbf{k}} W_{j\mathbf{k}}^2 D^{(0)}(\omega_{\mathbf{k}}) = d^{(0)}(\omega_j)^2 \Sigma^{(2)}(\omega_j), \tag{3.13}$$

with $\Sigma^{(2)}(\omega_j)$ being the second order self-energy.

First, we wish to limit our attention to the case of a nano-particle having a single mode. Obtaining the solution for a single mode we will relate it to FA result for the sake of illustration and then we will generalize our solution for the case of a nano-particle having multiple modes. Doing so, we will be able to take the interplay between neighboring modes during dissipation into account.

For a single nano-particle mode, the higher order terms can be expressed in terms of the second order self-energy and the free GF as

$$d(\omega_j, \omega_{\mathbf{q}}) = d^{(0)}(\omega_j, \omega_{\mathbf{q}}) \left(1 + d^{(0)}\Sigma^{(2)} + (d^{(0)}\Sigma^{(2)})^2 + ...\right). \tag{3.14}$$

For weak coupling, the above series can be written as

$$d(\omega_j, \omega_{\mathbf{q}}) \;=\; \frac{d^{(0)}(\omega_j, \omega_{\mathbf{q}})}{1 - d^{(0)}(\omega_j, \omega_{\mathbf{q}})\Sigma^{(2)}(\omega_j, \omega_{\mathbf{q}})}, \tag{3.15}$$

hence, the retarded GF becomes

$$d^R(\omega_j, \omega_{\mathbf{q}}) \;=\; \frac{1}{\omega_{\mathbf{q}} - \omega_j - \Sigma^{(2)}(\omega_j, \omega_{\mathbf{q}})}. \tag{3.16}$$

The real and imaginary parts of the second order self-energy can be separated

$$\Sigma^{(2)}(\omega_j, \omega_{\mathbf{q}}) = \mathbb{P} \int \frac{d\omega_{\mathbf{k}}\, g(\omega_{\mathbf{k}}) W_{j\mathbf{k}}^2}{\omega_{\mathbf{q}} - \omega_{\mathbf{k}}} - i\pi g(\omega_{\mathbf{q}}) W_{j\mathbf{q}}^2 \tag{3.17}$$

where $\mathbb{P}$ is for principal part of the integral, and the spectral function is obtained

$$A(j, \omega_{\mathbf{q}}) = \frac{-2\,\mathrm{Im}\,\Sigma^{(2)}(j, \omega_{\mathbf{q}})}{\left(\omega_{\mathbf{q}} - \omega_j - \mathrm{Re}\,\Sigma^{(2)}(j, \omega_{\mathbf{q}})\right)^2 + \left(\mathrm{Im}\,\Sigma^{(2)}(j, \omega_{\mathbf{q}})\right)^2}. \tag{3.18}$$

The real part of the second order self-energy $\Sigma^{(2)}$ is equal to the shift in the j^{th} mode of the nano-particle, σ_j, obtained previously using the FA method, and the square of the imaginary part of $\Sigma^{(2)}$ is $[\pi g(\omega_{\mathbf{q}}) W_{\mathbf{q}j}]^2$. That is, the FA expansion coefficient μ finds its expression in terms of the spectral function as

$$|\mu(\omega_{\mathbf{q}}, \omega_j)|^2 = \frac{A(j, \omega_{\mathbf{q}})}{2\pi g(\omega_{\mathbf{q}})}. \tag{3.19}$$

The time dependent GF can be written in terms of the spectral function and the time dependent occupancy of the j^{th} mode is obtained as

$$\langle n_j(t)\rangle = \langle n_j(0)\rangle \left| \int \frac{d\omega_{\mathbf{q}}}{2\pi} A(j,\omega_{\mathbf{q}})\, \mathrm{e}^{-i\omega_{\mathbf{q}}t} \right|^2 . \tag{3.20}$$

In order to incorporate the effect of neighboring modes, we follow diagrammatic technique. As long as the Hamiltonian is quadratic, the primitive vertex, from which all diagrams are to be constructed, will consist of two phonon lines. That is, each interaction point is the intersection of two phonon lines. Since the interaction Hamiltonian relates a nano-particle mode to a substrate mode only, each vertex contains one nano-particle phonon line and a substrate phonon line. So the diagram of any order can be constructed (see Fig. 3.2.b). Having obtained the diagrammatic expansion for any order $2n$, under certain conditions about the coupling type, the $(2n)^{th}$ order self-energy term can be expressed in terms of the second order term and the free GF of the nano-particle modes. If the fraction $W_{\mathbf{k}_1 j_1}/W_{\mathbf{k}_1 j_2}$ is independent of $\mathbf{k}_1$, self-energy for the multi-mode case can be found exactly where the fourth and sixth order contributions can be written as

$$\Sigma^{(4)}(j,\omega_q) = \frac{1}{W^2_{\mathbf{q}j}} \left(\sum_{j_1} d^{(0)}(j_1,\omega_q) W^2_{\mathbf{q}j_1} \right) \left(\Sigma^{(2)}(j,\omega_{\mathbf{q}})\right)^2 \tag{3.21}$$

$$\Sigma^{(6)}(j,\omega_q) = \frac{1}{W^4_{\mathbf{q}j}} \left(\sum_{j_1} d^{(0)}(j_1,\omega_q) W^2_{\mathbf{q}j_1} \right)^2 \left(\Sigma^{(2)}(j,\omega_{\mathbf{q}})\right)^3 \tag{3.22}$$

By mathematical induction, the $(2n)^{th}$ term is found as

$$\Sigma^{(2n)}(j,\omega_q) = \frac{1}{W^{2(n-1)}_{\mathbf{q}j}} \left(\sum_{j_1} d^{(0)}(j_1,\omega_q) W^2_{\mathbf{q}j_1} \right)^{n-1} \left(\Sigma^{(2)}(j,\omega_{\mathbf{q}})\right)^n , \tag{3.23}$$

and hence,

$$\Sigma(j,\omega_{\mathbf{q}}) = \frac{\Sigma^{(2)}(j,\omega_{\mathbf{q}})}{1 - \frac{\Sigma^{(2)}(j,\omega_{\mathbf{q}})}{W^2_{j\mathbf{q}}} \sum\limits_{j'\neq j} W^2_{j'\mathbf{q}} d^{(0)}(j',\omega_{\mathbf{q}})}. \tag{3.24}$$

Once the self-energy is found, the spectral function, therefore the time dependent occupancy of the nano-particle modes can be calculated.

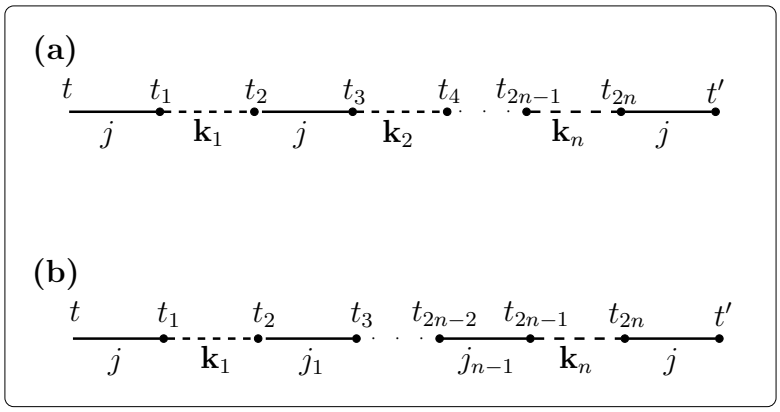

Figure 3.2: Diagrams of order $2n$. Solid lines are the phonon lines of the nano-particle where the dashed lines are that of the substrate. (a) Diagram for the case of single nano-particle mode, j. $\mathbf{k}_i$ stand for the substrate modes. (b) Diagram of order $2n$ when there exists multiple modes (j_i) for the nano-particle.

A few remarks about the above expression for the self-energy follow. First, it is exact in the sense that it includes contributions from diagrams to all orders. Second $\Sigma(j, \omega_{\mathbf{q}})$ is not a quadratic function of coupling $W_{\mathbf{k}j}$ anymore, as it was in the single mode approximation case. Rather, the decay rate of j^{th} mode collects contributions from all other modes also. Third, the spectral function is not of Lorentzian shape anymore; extra peaks and dips in the spectral function are in question which will be analyzed numerically in the following section.

3.3 Results and Discussions

In this section, we will apply the above methods using Lorentzian and square-root coupling to analyze the dependence of the decay rate on the properties of nano-particles and substrates having 1D, 2D Debye DOS. The analytical results obtained using EoM technique and numerical results obtained using FA and GF methods are discussed separately. An application for a real physical system using DFT and the GF method will also be presented.

As an application of the EoM method, we consider the nano-particle that has

single mode coupled to a 1D or 2D Debye substrate. The substrate is initially at zero temperature. Assuming Lorentzian coupling, namely

$$W_{\mathbf{k}j}^2 = \frac{\alpha^2\Gamma}{2\pi}\frac{1}{(\omega_{\mathbf{k}}-\omega_j)^2+\Gamma^2/4}, \tag{3.25}$$

we have for $I_j(s)$ (see Appendix C)

$$I_j = \frac{\alpha^2\Gamma c_D}{2\pi i}\int_0^{\omega_{max}} \frac{d\omega_{\mathbf{k}}\,\omega_{\mathbf{k}}^{d-1}}{(\omega_{\mathbf{k}}-is)(\omega_{\mathbf{k}}-\omega_j-i\frac{\Gamma}{2})(\omega_{\mathbf{k}}-\omega_j+i\frac{\Gamma}{2})}, \tag{3.26}$$

where d is the dimension of the substrate, c_D is the corresponding Debye constant for DOS, $g_d(\omega) = c_D\omega^{d-1}$. ω_j, Γ are real and positive, and by definition of Laplace transformation $\mathrm{Re}(s) > 0$. In the weak coupling regime the width of the Lorentzian will be much smaller than ω_j and ω_{max}, [68] so we can approximate the above integral by extending the limits of integration to $(-\infty,\infty)$ in which case the integral can be evaluated analytically on the complex $\omega_{\mathbf{k}}$-plane with the result $I_j(s) = \alpha^2 c_D\,(\omega_j - i\Gamma/2)^{d-1}\,/\,(s+i\omega_j+\Gamma/2)$. Performing the inverse transformation, one finds

$$\langle n_j(t)\rangle = \langle n_j(0)\rangle\frac{\mathrm{e}^{-\Gamma t/2}}{4|\Delta|^2}\times\left|(\Gamma+\Delta)\,\mathrm{e}^{\Delta t/2}-(\Gamma-\Delta)\,\mathrm{e}^{-\Delta t/2}\right|^2$$

where $\Delta^2 = \Gamma^2/4 - 4\alpha^2 c_D(\omega_j - i\Gamma/2)^{d-1}$.

It is noted that the domain of applicability of the EoM technique is quite limited due to the fact that inverse Laplace transformation is not always possible neither analytically nor numerically. Nevertheless, in certain cases the EoM method enables us to get analytical results within some approximations. Fig. 3.3 shows the decay of a single nano-particle mode to a 2D-Debye substrate obtained by the EoM method. The oscillatory behavior is due to the splitting of the molecular spectrum into two.

Next, using FA and GF methods, we discuss the critical features in the dissipation of single mode energies of nano-particle to 1D and 2D substrates. In the weak coupling regime, the width of the spectral function $A(j,\omega_{\mathbf{q}})$ will be small compared to $\omega_{\mathbf{q}}$ provided that ω_j is not close to zero, which is already

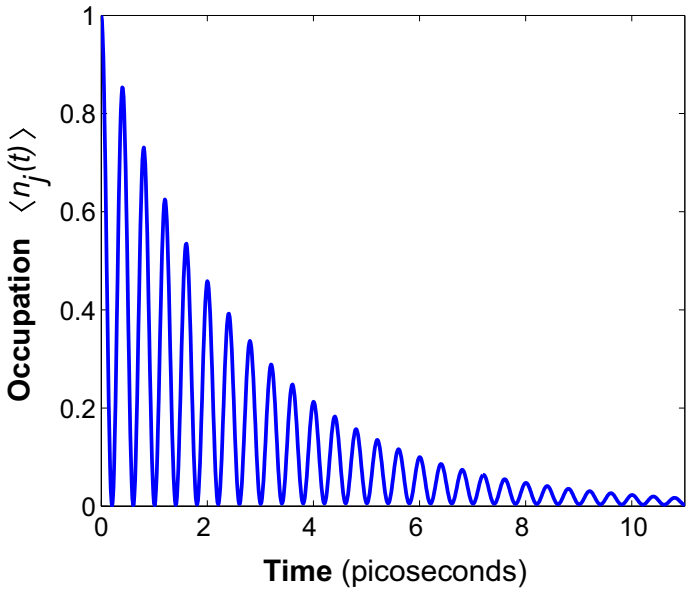

Figure 3.3: Decay of a single nano-particle mode j coupled to a 2D-Debye substrate. The coupling is Lorentzian. Occupation $\langle n_j(t) \rangle$ at time t is given relative to the initial occupation $\langle n_j(0) \rangle$.

satisfied for nano-particles. In this limit, the imaginary part of the self-energy can be interpreted as twice the decay rate, $\gamma_j = \mathrm{Im}\,\Sigma(j, \omega_{\mathbf{q}})/2$. Therefore, the dependence of decay rate on the interaction type and strength as well as on the frequency of the nano-particle can be obtained from the spectral function.

For the case of Lorentzian coupling, the interaction strength α is linear with $W_{\mathbf{k}j}$, which shows that the decay rate increases with α^2. If the coupling is only a function of the distance between interacting atoms of the substrate and the nano-particle, the coupling has the form of Eq. (3.6) with α being proportional to a spring constant k_{int} connecting the interacting atoms. Since the spectral function scales with α^2, decay rate increases with k_{int}^2 for inverse-square-root coupling case. The k_{int}^2 law was previously obtained using elastic continuum model for phononic dissipation in physisorption systems [69].

The dependence on the nano-particle mode frequency is a key issue we

wish to emphasize in phononic energy dissipation. In Lorentzian coupling case, the decay rate is determined by the width of the Lorentzian rather than the frequency. On the other hand, for inverse-square-root coupling (cf. Eq. (3.6)), it is inversely proportional to the nano-particle mode frequency ω_j. It is evident from equations (D.12) and (3.18) that phonons in mode ω_j decay faster as the substrate DOS at the center of the peak, $\omega_j - \mathrm{Re}\,\Sigma(j, \omega_{\mathbf{q}})$, increases. A crucial consequence of dependence on substrate DOS is that, if the DOS at the peak of the spectral function tends to zero, the spectral function (and $|\mu(\omega_{\mathbf{q}}, \omega_j)|^2$) has the form of a δ-function. In the language of dressed modes, this corresponds to a localized mode, i.e. it does not decay at all. Such localized states are also known to occur in e.g. solid state physics [66] and atomic physics [65]. For weak coupling, the real part of the self-energy is small, so the peak of the spectral function is not altered significantly from its original position ω_j. In other words, lying outside the continuum of substrate modes, it is unlikely to be shifted into the range where it can decay or vice versa. Decay of such localized modes is possible, on the other hand, by including the anharmonic terms in the Hamiltonian. Localized modes of the harmonic approximation now will gain finite width due to multi-phonon interactions. In general, three-phonon interactions are weak, four-phonon processes are even weaker, and the first nonzero contribution from three-phonon processes arise at the second-order term of the diagrammatic expansion. Another mechanism for decay of localized harmonic modes can be due to double annihilation/creation terms in the interaction Hamiltonian which are neglected in this study (cf Eqn. 3.4). Namely, though localized modes are not truly localized considering anharmonic terms or double annihilation/creation terms, their decay rates will be small. Another important effect about DOS dependence takes place when the spectral peak coincides with a van-Hove singularity of the substrate DOS, by which the decay rate is enhanced abruptly.

We also investigate the effect of a neighboring mode within square-root coupling in 1D and 2D Debye substrate densities of states using GF method. We consider four nano-particle modes, $\omega_1 = 0.7\,\omega_{max}$, $\omega_2 = 0.65\,\omega_{max}$, $\omega_3 = 0.55\,\omega_{max}$ and $\omega_4 = 0.45\,\omega_{max}$. The effect is analyzed pairwise, namely, we

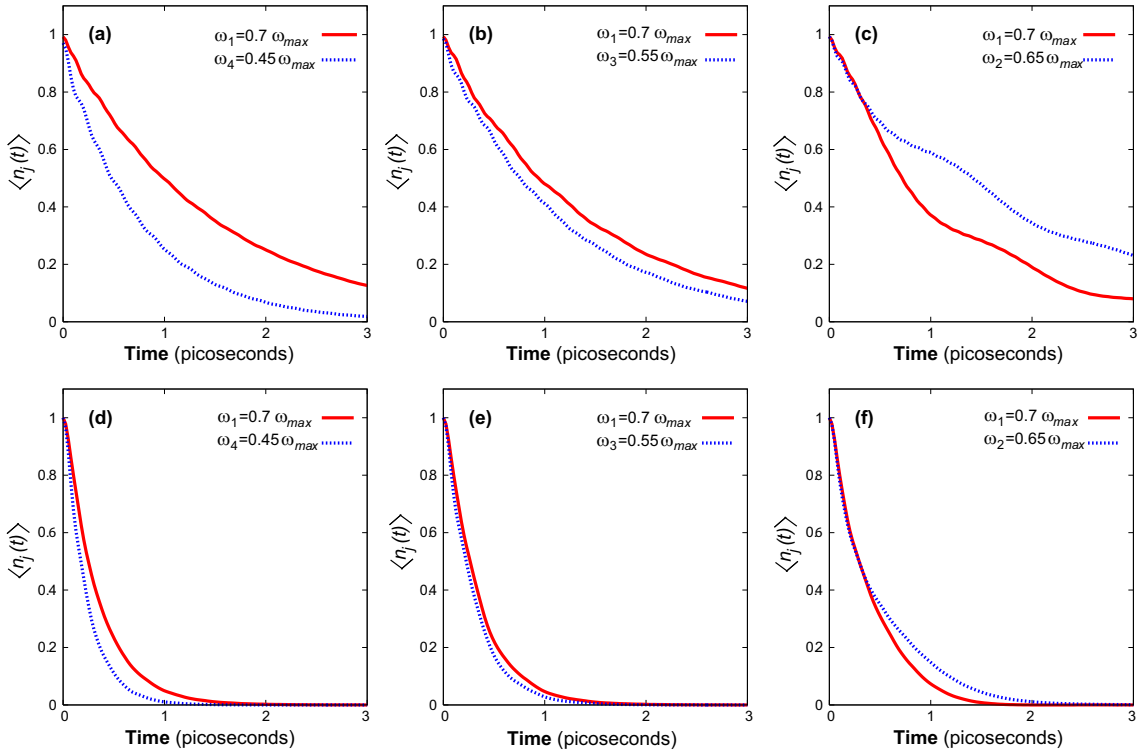

Figure 3.4: Effect of neighboring modes. Figures (a), (b), (c) are for 1D-Debye DOS, and (d), (e), (f) are for 2D-Debye DOS with nano-particle vibration frequencies $\omega_1 = 0.7\,\omega_{max}$, $\omega_2 = 0.65\,\omega_{max}$, $\omega_3 = 0.55\,\omega_{max}$, $\omega_4 = 0.45\,\omega_{max}$. Figures (a) and (d), (b) and (e) and (c) and (f) show dissipation of phonon occupation for the pairs (ω_1, ω_4), (ω_1, ω_3), and (ω_1, ω_2) respectively.

consider (ω_1, ω_2), (ω_1, ω_3) and (ω_1, ω_4) as the nano-particle modes keeping other parameters unchanged. That is, we keep ω_1 constant while changing the second mode and investigate dependence of decay of ω_1-mode on the separation from the second nano-particle mode. For both 1D-Debye (Fig. 3.4 (a) (b) and (c)) and 2D-Debye (Fig. 3.4 (d), (e), and (f)) cases we observe that the decay of excited modes gain a retardation as the mode frequencies get closer. A second behavior is the enhancement of fluctuations during decay as the mode frequencies get closer. Both behaviors can be understood in terms of the spectral functions. In Fig. 3.5(a) spectral functions of ω_1- and ω_3-modes are plotted for single-mode (dashed curves) and multi-mode (solid curves) obtained using GF calculations. It is seen that the overlap is negligible and the spectra are not changed considerably. When the modes are closer (Fig. 3.5.b) the single-mode spectra (dashed curves) have finite overlap, correspondingly the multi-mode spectral functions effect each other. The Lorentzian shape is distorted and the peak of ω_2-mode is enhanced. These result in retardation and fluctuations during decay. More precisely, the finite overlap of spectra allows the nano-particle to gain phonons back which are previously discharged to the substrate. This phonon exchange process continues during the dissipation and gives rise to retardations and fluctuations observed in Fig. 3.4.

In order to provide a comparison of the results obtained from the quantum treatment with those obtained by classical treatment we carry out calculations using classical Molecular Dynamics Method. We use a simple but effective approach, where we consider the nano-particle/substrate as a cluster/lattice of masses and harmonic springs in the first nearest neighbor approximation, and with the lattice having different dimensionalities. The interaction is described by a harmonic spring between an atom of the nano-particle and a substrate atom. Using the dynamical matrix, the eigenmodes of the isolated nano-particle are determined and initial energy is loaded to desired modes by giving the initial velocities to the atoms in correspondence with the modes. In the presence of the interaction between the nano-particle and the substrate, the differential equations and hence the motion of atoms are determined in discrete time steps which are

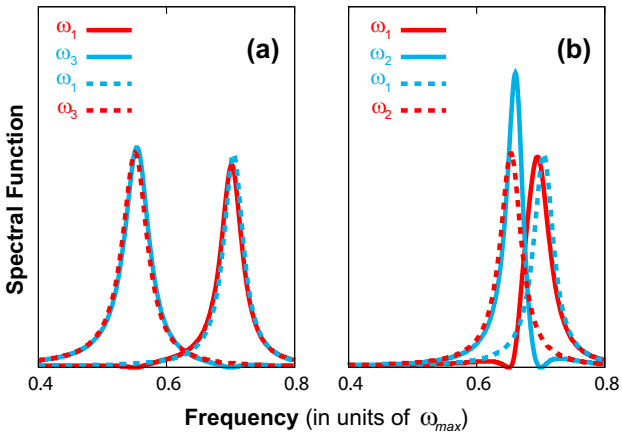

Figure 3.5: Effect of a neighboring mode on the spectral function. Dashed curves are the single mode spectral functions whereas the solid curves are spectral functions in the existence of a neighboring mode. (a) Spectra of $\omega_1 = 0.7\,\omega_{max}$ and $\omega_3 = 0.55\,\omega_{max}$ for both cases are almost the same. (b) Spectra of $\omega_1 = 0.7\,\omega_{max}$ and $\omega_2 = 0.65\,\omega_{max}$ get narrowed and distorted when single mode condition is relaxed.

on the order of a femtosecond. Since the classical version of the problem, which is stated above, is not an exact analog to the quantum one, and due to quantum versus classical natures of the two, we compare and contrast the basic features of the results emerging from them.

In agreement with the earlier prediction based on the elastic continuum model [69], and with the result previously obtained using the single mode, the dependence of decay rate on the interaction strength obeys k_{int}^2 law for weak coupling. Likewise, the dependence on vibrational mode frequency verifies the previously obtained result, namely keeping the coupling strength constant, higher frequency modes decay slower. We should note that the substrate DOS in the neighborhood of the nano-particle mode frequency also affects the decay rates. Using a 1D substrate and choosing the nano-particle modes away from the maximum frequency of the substrate, the effect of substrate DOS is minimized. Although the density of substrate phonon modes is higher for higher frequencies, the decay rate decreases due to nano-particle mode frequency dependence.

Another property of the dissipation process becomes apparent when the dynamics is analyzed for a nano-particle having one and two vibrational modes. We consider a diatomic molecule and a linear triatomic molecule, which have one and two vibrational modes along the molecular axis, where the interaction is also along the molecular axis. The effect of neighboring mode can be analyzed by setting one of the modes of the triatomic molecule at the same frequency with the frequency of the diatomic one. Exciting only the common frequency of both diatomic and triatomic molecules, we compare the decay rates keeping the interaction and substrate parameters fixed. In the weak coupling regime, it is observed that the decay rate of the common mode does not change appreciably. Moreover, exciting both vibrational modes of the triatomic molecule does not effect the decay rate of the common mode to a great extend. This property becomes more apparent when the coupling strength is weakened. Since the vibrational modes of a triatomic molecule along the molecular axis are well-separated, this result is expected in the light of GF solution of the quantum Hamiltonian. The mode localization effect is also tested using classical MD simulations. Unlike the quantum solution, a molecular mode whose frequency lies above the maximum frequency of the substrate has a small but yet finite decay rate.

Finally we present a specific and more realistic study of energy dissipation from the excited modes of a benzene (C_6H_6) molecule coupled to graphene using GF method. Here the multi-mode frequencies of C_6H_6, the continuous phonon spectrum of graphene and the coupling between them are calculated by using first-principle ultra-soft pseudopotential[70] plane wave method[26] within DFT[21]. The exchange correlation potential has been approximated by Generalized Gradient Approximation (GGA) [71] using PW91 [72] functional.

These calculations allow an accurate quantum mechanical treatment. All atomic positions are optimized by the conjugate gradient method and the system is considered to be at equilibrium when Hellman-Feynman forces are below 10 meV/Å. A large supercell is used for the free C_6H_6 molecule so that the distance

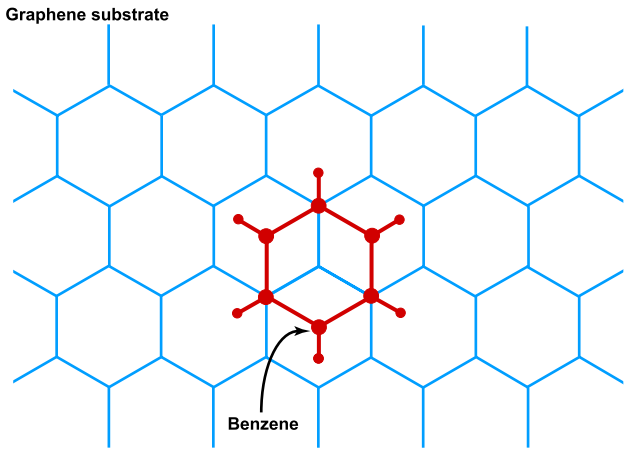

Figure 3.6: Relaxed geometry of benzene on graphene. Blue (gray) lines show the graphene structure.

to the nearest atom of the neighboring C_6H_6 molecule is above 10 Å. A plane-wave basis set with kinetic energy cut-off $\hbar^2|\mathbf{k}+\mathbf{G}|^2/2m = 350$ eV has been used. Each atom is shifted by 0.01 Å in each direction from their equilibrium positions, and the resulting forces on each atom are used to construct the dynamical matrix such that

$$K^{\mu\nu}_{\alpha\beta} = \frac{1}{2}\frac{F^{\mu\nu+}_{\alpha\beta} - F^{\mu\nu-}_{\alpha\beta} + F^{\nu\mu+}_{\beta\alpha} - F^{\nu\mu-}_{\beta\alpha}}{2d} \tag{3.27}$$

where $F^{\mu\nu\pm}_{\alpha\beta}$ denotes the force on atom β along ν when αth atom is moved along μ in positive or negative direction; d is the displacement imposed on a specific atom. The dynamical matrix is defined in terms of these forces as $D_{ij} = D_{3(\alpha-1)+\mu,3\beta-1+\nu} = K^{\mu\nu}_{\alpha\beta}$. Solving the dynamical matrix, the vibration frequencies and the corresponding normal coordinates are determined.

The interaction between the C_6H_6 molecule and the underlying graphene is calculated by relaxing the geometry in a supercell of the same size used for free C_6H_6, the final geometry is schematically shown in Fig. 3.6. The equilibrium distance between the molecule and graphene is 3.75 Å, that is the interaction is weak. For the sake of simplicity, we assume that the interaction between the molecule and the substrate is achieved by the C-atoms lying on top of each other,

Table 3.1: The out-of-plane vibrational modes of C_6H_6 and the effective coefficients which scale the coupling strength.

	Frequency ω_j(THz)	**Effective Coefficient c_j**
1	11.99	0.962
2	11.99	0.962
3	20.58	0.301
4	21.39	1.105
5	26.03	0.489
6	26.03	0.489
7	29.66	0.566
8	29.66	0.566
9	30.12	0.528

and varying the benzene-graphene distance vertically we obtain a total energy versus distance curve to which we perform a quadratic fit to calculate this effective interaction constant. The interaction constant between C-atoms lying on top of each other is found to be 13.55 eV/Å^2.

Since the interaction is weak and the C_6H_6-graphene distance is large, the dissipation will occur mostly through the out-of-plane motions of C_6H_6 atoms due to their coupling to the transverse modes of graphene. Using the normal coordinates of these vibrational modes, the contribution of each atom to the interaction can be determined. When a single atom of the molecule is interacting with the substrate, the coupling coefficient goes like $W_{\mathbf{k}j} = c\,\omega_{int}^2/\sqrt{\omega_{\mathbf{k}}\omega_j}$, where ω_j stands for the frequency of j^{th} mode of the molecule, c is the normal coordinate of the interacting atom in j^{th} mode. When there are more than one atoms interacting with the substrate (as is the case for C_6H_6-graphene), we sum over those interacting degrees of freedom to find the effective coefficient c which scales the coupling strength. The out-of-plane vibrational modes of benzene and the scaling coefficients are given in Table 3.1. It is worth mentioning that C_6H_6 has doubly-degenerate modes which is due to hexagonal symmetry of the molecule, i.e. (1,2), (5,6), (7,8) of Table 3.1 form degenerate pairs for free C_6H_6. The coefficients of the degenerate modes are identical due to symmetry grounds.

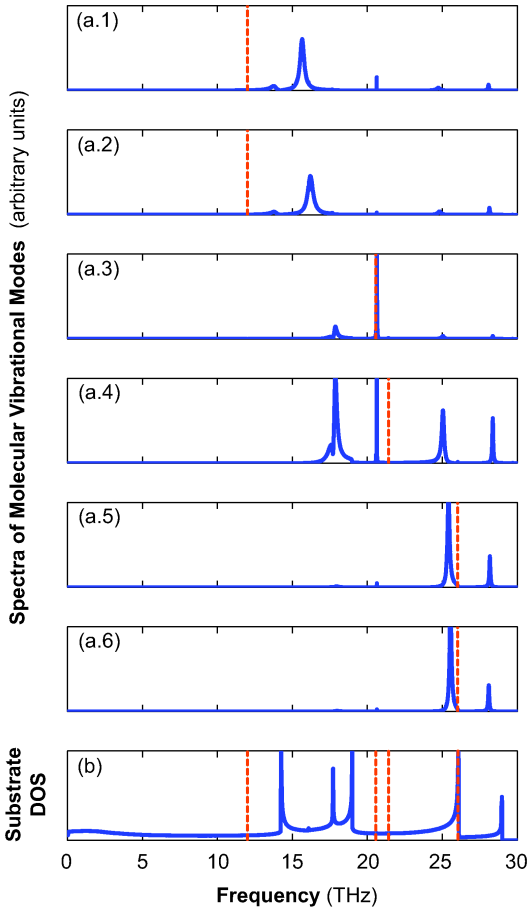

Figure 3.7: Spectra of the six lowest lying vibrational modes of benzene when interacting with a graphene sheet (a.1-6), and DOS of transverse phonons of the graphene substrate (b). The dashed lines indicate the vibrational frequencies of the free benzene molecule.

The spectral function $A(j, \omega_{\mathbf{q}})$ for each mode is calculated using the GF method. Since only the lowest six of the out-of-plane mode frequencies lie within the range of transverse substrate phonons, they gain a finite width while remaining three modes stay localized. The spectra of the lowest lying modes and the DOS of transverse substrate phonons are shown in Fig. 3.7. The coupling strengths of degenerate modes are equal therefore their spectral functions are identical. Dependence of the shift and broadening of the spectral function on the coupling coefficient manifests itself as the narrow spectral peak of the third mode when compared to that of the first two modes. Altough third and fourth modes are close to each other, the dissipation of the fourth one is much faster than that of third mode. The broadening of fifth and sixth modes would be much larger if their shifted peaks were matched the singularity of the DOS near 26 THz. But they gain a shift which pushes the peak far from the singularity. We observe that there might appear more than one peaks in the spectrum of a single mode. This is due to two reasons, the contributions from the singularities in the substrate DOS, and the interaction stimulated anharmonicities within the molecule. Altough the molecule is treated in the harmonic approximation, interaction Hamiltonian gives rise to an indirect coupling between different vibrational modes of the free molecule.

Chapter 4

Conclusions

Graphene is a unique system in a number of respects. Not only by being a truly two-dimensional crystal, but also due to the unusual electronic excitations described as massless Dirac fermions. It is worthy to note that graphene can easily be obtained from graphite which makes it a readily available material for basic research, and frees us from expensive sample growth techniques.

The electronic structure of graphene resembles a mix of a semiconductor by having zero density of states at the Fermi level, and a metal by being gapless. More interestingly, these properties can easily be modified through adsorption or by control of its geometry as it is argued theoretically in this thesis.

The other focus of this thesis, the phononic dissipation problem, plays an important role in many physical phenomena which range from everyday experience such as sliding friction and boundary lubrication to sophisticated experimental techniques like atomic force microscopy or infrared Raman spectroscopy. Owing to the advances in experimental techniques and the accessibility of nanoscale sizes, a fully quantum mechanical approach to the heat discharge and phononic dissipation problems becomes more significant.

The results we obtained can be summarized as follows. In Chapter 2, we first investigated $3d$-transition metal adsorption on graphene and armchair graphene nanoribbons. For graphene it is found that adsorption on the hollow site gives the minimum energy for all TM-atoms we examined except for Cr. The possibility

of dimerization of two TM-atoms adsorbed on adjacent unit cells for AFM states is also investigated. For Ti, Co and Fe dimerization is weaker whereas for Mn and Cr it is more pronounced. The same applies to AGNRs where the edge hollow site yields the minimum energy. Upon TM-atom adsorption semimetallic bare graphene can change to a ferromagnetic or antiferromagnetic metal. The electronic and magnetic properties of TM-atom adsorbed armchair graphene nanoribbons show variations depending on the adsorbate concentration, adsorption site and the species of TM elements. In general their magnetic states are more robust for strongly binding species in the sense that their magnetic properties are less altered by the ribbon width. This makes them candidates for future applications especially for wider ribbons. Also zigzag chain formation of adsorbed TM-atoms at the ribbon edge makes AGNRs an interesting system for studying magnetism in one dimension. Presenting a short review of the electronic properties of graphene nanoribbons, we investigated the electronic structure and the magnetic state of zigzag graphene ribbons when their widths are modulated periodically in real space. We showed that spins can be confined in quantum wells, and the antiferromagnetic ribbon can change to a ferrimagnetic semiconductor. Since a finite superlattice with desired geometry can now be produced from graphene sheet by chemical methods [29], the modulation of electronic and magnetic states, and confined spins hold the promise for the fabrication of interesting nanodevices. For example, by applying a gate voltage through an electrode to a graphene sheet over an oxide layer, one can also generate the desired geometry. The electronic and magnetic properties of superlattices revealed in this study can be realized in future spintronic applications. In the last section of Chapter 2, a resonant tunneling double barrier device is proposed by where the barrier and the well regions are obtained by the modulation of the width of armchair graphene nanoribbons. It is found that confined states in the wider segment of the ribbon serve as quantum well states which give rise to sharp peaks in the transmission spectrum, whereas the remaining energy levels broaden significantly and are shifted away from the Fermi level due to the contact with the electrodes.

In Chapter 3, the phononic dissipation from a nano-structure weakly coupled to a substrate has been analyzed using three different methods. It is shown that the equation of motion technique is able to yield analytical results, but has a limited range of applicability because of the fact that inverse Laplace transformation is not always possible. On the other hand, Fano-Anderson diagonalization is possible for any type of substrate density of states and any type of coupling, but is restricted to considerations of single nano-particle mode only. Using Green's functions, the effect of neighboring nano-particle modes can also be investigated. It is found that stronger the coupling, faster is the rate of dissipation. Since the width of the spectrum of a single nano-particle mode scales with the value of the substrate DOS at the shifted frequency of the nano-particle mode, we observe that a single nano-particle mode coupled to a 2D-Debye substrate decays faster than the one coupled to a 1D-Debye substrate. This situation can be reversed for those frequencies for which 1D-DOS is higher than the 2D-DOS, namely for low frequencies (larger nano-particles). That is, at frequencies at which 1D-DOS has higher values than 2D-DOS, decay rate of a mode coupled to the 1D substrate will be higher than that of the mode coupled to 2D substrate provided that the remaining factors are kept identical. Presence of neighboring nano-particle modes effect each other's decay rate when their spectral functions have an appreciable overlap. Transitions between nano-particle modes take place via the substrate modes, therefore retardation as well as fluctuations become important when the modes are close enough. Furthermore, using the results obtained from a first-principles study, interplay between molecular modes depending on the substrate DOS is demonstrated. Using the formalism developed we studied energy from a benzene molecule to graphene substrate.

Appendix A

Details of Density Functional Calculations

In calculating the electronic and magnetic properties using density functional theory [21], projector augmented wave (PAW) [27] approach within a PW91 [72]-GGA [71] approximation for the exchange and correlation functional is used as currently implemented in the VASP [26] software. For phonon calculations ultra-soft pseudopotentials [70] are used. Geometry optimizations are performed by allowing all atomic positions to vary, for bulk structures all cell parameters are optimized as well. The atomic positions are optimized by the conjugate gradient method, and the system is considered to be at equilibrium when Hellman-Feynman forces are below 10 meV/Å. Monkhorst-Pack meshes with sufficient number of k-points are used to converge the energies. For one-dimensional and two-dimensional structures, the minimum size of the implemented k-point meshes are $(21, 1, 1)$ and $(11, 11, 1)$, respectively. Periodic boundary conditions are implemented in all directions, where sufficiently large vacuum (minimum of 10 Å) is inserted in directions without crystal symmetry in order to prevent artificial interactions. The kinetic energy cut-off for the plane wave basis set is chosen as $\hbar^2|\mathbf{k} + \mathbf{G}|^2/2m = 500$ eV when using PAW potentials and 350 eV when using ultrasoft pseudopotentials. The convergence criterion for electronic relaxations has been set to 10^{-5} eV for all cases.

Appendix B

Details of Green's Function Calculations for Semi-infinite Electrodes

In this appendix the surface Green's function matching method [73, 74] for obtaining the free electrode Green's functions is summarized. For a one-dimensional semi-infinite system (here the right electrode), the Hamiltonian and the overlap matrices are band diagonal and have the form

$$H = \begin{pmatrix} H_{00} & H_{01} & 0 & \\ H_{01}^{\dagger} & H_{00} & H_{01} & \cdots \\ 0 & H_{01}^{\dagger} & H_{00} & \\ & \vdots & & \ddots \end{pmatrix}, \qquad S = \begin{pmatrix} S_{00} & S_{01} & 0 & \\ S_{01}^{\dagger} & S_{00} & S_{01} & \cdots \\ 0 & S_{01}^{\dagger} & S_{00} & \\ & \vdots & & \ddots \end{pmatrix}. \quad \text{(B.1)}$$

It is important to note that, without loosing generality the cells are chosen such that they include enough number of layers to prevent second nearest neighboor interactions. Defining the Green's function as $g = [\epsilon S - H]^{-1}$, we write

$$\begin{pmatrix} \epsilon S_{00} - H_{00} & \epsilon S_{01} - H_{01} & \\ \epsilon S_{01}\dagger - H_{01}^{\dagger} & \epsilon S_{00} - H_{00} & \cdots \\ 0 & \epsilon S_{01}\dagger - H_{01}^{\dagger} & \\ & \vdots & \ddots \end{pmatrix} \cdot \begin{pmatrix} g_{00} & g_{01} & g_{02} & \\ g_{10} & g_{11} & g_{12} & \cdots \\ g_{20} & g_{21} & g_{22} & \\ & \vdots & & \ddots \end{pmatrix} = \mathbb{1} \quad \text{(B.2)}$$

Multiplication of the first row with the first column yields

$$(\epsilon S_{00} - H_{00})g_{00} + (\epsilon S_{01} - H_{01})g_{10} = \mathbb{1}, \tag{B.3}$$

similarly, the second row with the first column gives

$$(\epsilon S_{00} - H_{00})g_{10} + (\epsilon S_{01}^{\dagger} - H_{01}^{\dagger})g_{00}(\epsilon S_{01} - H_{01})g_{20} = 0, \tag{B.4}$$

and hence the nth row with the first column gives

$$(\epsilon S_{00} - H_{00})g_{n,0} + (\epsilon S_{01}^{\dagger} - H_{01}^{\dagger})g_{n-1,0} + (\epsilon S_{01} - H_{01})g_{n+1,0} = 0. \tag{B.5}$$

Here one can define translation operators T and $\bar{T}$ such that

$$g_{10} = Tg_{00}, \qquad\qquad g_{00} = \bar{T}g_{10}, \tag{B.6}$$

by which the important piece of the Green's function can be expressed as $g_{00} = [\epsilon S_{00} - H_{00} + (\epsilon S_{01} - H_{01})T]^{-1}$.

In order to find T, we follow an iterative approach. Defining

$$t_0 = -(\epsilon S_{00} - H_{00})^{-1}(\epsilon S_{01}^{\dagger} - H_{01}^{\dagger}), \tag{B.7}$$

$$\tilde{t_0} = -(\epsilon S_{00} - H_{00})^{-1}(\epsilon S_{01} - H_{01}), \tag{B.8}$$

Eqn. (B.5) can be written as $g_{n0} = t_0 g_{n-1,0} + \tilde{t_0} g_{n+1,0}$. Iterating once, we write $g_{n0} = t_1 g_{n-2,0} + \tilde{t_1} g_{n+2,0}$ with

$$t_1 = \left(1 - t_0\tilde{t_0} - \tilde{t_0}t_0\right)^{-1} t_0^2, \tag{B.9}$$

$$\tilde{t_1} = \left(1 - t_0\tilde{t_0} - \tilde{t_0}t_0\right)^{-1} \tilde{t_0}^2. \tag{B.10}$$

By induction, further iterations can be obtained as

$$g_{n0} = t_m g_{n-2^m,0} + \tilde{t}_m g_{n+2^m,0}, \tag{B.11}$$

$$t_m = \left(1 - t_{m-1}\tilde{t}_{m-1} - \tilde{t}_{m-1}t_{m-1}\right)^{-1} t_{m-1}^2, \tag{B.12}$$

$$\tilde{t}_m = \left(1 - t_{m-1}\tilde{t}_{m-1} - \tilde{t}_{m-1}t_{m-1}\right)^{-1} \tilde{t}_{m-1}^2, \tag{B.13}$$

and using these relations repeatedly, one obtains

$$g_{10} = \left(t_0 + \tilde{t}_0 t_1 + \tilde{t}_0\tilde{t}_1 t_2 + \cdots + \tilde{t}_0 \cdots \tilde{t}_{n-1} t_n\right) g_{00} + \tilde{t}_0\tilde{t}_1 \cdots \tilde{t}_n g_{2^{n+1},0}. \tag{B.14}$$

The process is repeated until t_{n+1} and $\tilde{t}_{n+1}$ are smaller than small positive number which determines the accuracy of the calculation. Hence the second term yields zero, and the translation operator finds its expression as

$$T = \left(t_0 + \tilde{t}_0 t_1 + \tilde{t}_0 \tilde{t}_1 t_2 + \cdots + \tilde{t}_0 \cdots \tilde{t}_{n-1} t_n\right). \tag{B.15}$$

Considering the right electrode Hamiltonian defined in Eqn. (B.1), the self energy is $\Sigma_R = H_{01} T$, whereas for the left electrode it is $\Sigma_L = H_{01}^{\dagger} \bar{T}$.

Appendix C

Details of Equation of Motion Technique

The Laplace transformed form of equations of motion are (see equations 3.7 and 3.8)

$$\overline{a}_l(s)(s + i\omega_l) = a_l(0) - i\sum_{\mathbf{k}} W^*_{\mathbf{k}l}\overline{b}_{\mathbf{k}}(s), \tag{C.1}$$

$$\overline{b}_{\mathbf{k}}(s)\,(s + i\omega_{\mathbf{k}}) = b_{\mathbf{k}}(0) - i\sum_{j} W_{\mathbf{k}j}\overline{a}_j(s), \tag{C.2}$$

where s is the Laplace frequency. Solving for $\overline{a}_l(s)$, one obtains

$$\overline{a}_l(s) = \frac{a_l(0)}{s + i\omega_l} - i\sum_{\mathbf{k}} \frac{W^*_{\mathbf{k}l} b_{\mathbf{k}}(0)}{(s + i\omega_{\mathbf{k}})(s + i\omega_l)} - \sum_{\mathbf{k}j} \frac{W^*_{\mathbf{k}l} W_{\mathbf{k}j}\overline{a}_j(s)}{(s + i\omega_{\mathbf{k}})(s + i\omega_l)}. \tag{C.3}$$

Considering the couplings to be non-overlapping (cf. Eqn. (3.5)) we are left with the relation

$$\overline{a}_l(s) = \frac{a_l(0)}{s + i\omega_l + \sum_{\mathbf{k}} \frac{|W_{\mathbf{k}l}|^2}{s+i\omega_{\mathbf{k}}}} - i\frac{\sum_{\mathbf{k}} \frac{W^*_{\mathbf{k}l} b_{\mathbf{k}}(0)}{s+i\omega_{\mathbf{k}}}}{s + i\omega_l + \sum_{\mathbf{k}} \frac{|W_{\mathbf{k}l}|^2}{s+i\omega_{\mathbf{k}}}} \tag{C.4}$$

Having obtained $\overline{a}_l(s)$ in terms of $a_l(0)$ and $b_{\mathbf{k}}(0)$, the inverse Laplace transform will yield $a_l(t)$, thus we can obtain the time dependent occupancy of the l^{th} mode.

We convert the summations into integrals over the substrate modes, and denote them as

$$I_l(s) = \sum_{\mathbf{k}} \frac{|W_{\mathbf{k}l}|^2}{s + i\omega_{\mathbf{k}}} = \int \frac{d\omega_{\mathbf{k}}\, g(\omega_{\mathbf{k}})\, |W_{\mathbf{k}l}|^2}{s + i\omega_{\mathbf{k}}} \tag{C.5}$$

$$J_l(s) = \sum_{\mathbf{k}} \frac{W^*_{\mathbf{k}l} b_{\mathbf{k}}(0)}{s + i\omega_{\mathbf{k}}} = \int \frac{d\omega_{\mathbf{k}}\, g(\omega_{\mathbf{k}})\, W^*_{\mathbf{k}l} b_{\mathbf{k}}(0)}{s + i\omega_{\mathbf{k}}} \tag{C.6}$$

where $g(\omega_{\mathbf{k}})$ is the phonon density of states for the substrate, I_l and J_l depend on s, and J_l is an operator. We can write Eqn. (C.4) as

$$\overline{a}_l(s) = \frac{a_l(0)}{s + i\omega_l + I_l(s)} - i\frac{J_l(s)}{s + i\omega_l + I_l(s)} \tag{C.7}$$

The inverse transform of $\overline{a}_l(s)$ is

$$a_l(t) = \frac{a_l(0)}{2\pi i} \oint_B \frac{e^{st} ds}{s + i\omega_l + I_l(s)} - \frac{1}{2\pi} \oint_B \frac{e^{st} J_l(s) ds}{s + i\omega_l + I_l(s)} \tag{C.8}$$

Appendix D

Details of Fano-Anderson Method

Since the bare phonon operators a_j, $b_{\mathbf{k}}$ form a complete set of operators for the combined system, the dressed operators $\alpha(\omega_{\mathbf{q}})$ can be expanded in terms of the bare operators as

$$\alpha(\omega_{\mathbf{q}}) = \sum_j \mu(\omega_{\mathbf{q}}, \omega_j) a_j + \sum_{\mathbf{k}} \nu(\omega_{\mathbf{q}}, \omega_{\mathbf{k}}) b_{\mathbf{k}} \tag{D.1}$$

and they satisfy the eigenoperator equation $[\alpha(\omega_{\mathbf{q}}), H] = \hbar\omega_{\mathbf{q}}\, \alpha(\omega_{\mathbf{q}})$. Conversely, we find the bare operators by the following expressions in terms of the dressed operators as

$$a_j = \sum_{\mathbf{q}} \mu^*(\omega_{\mathbf{q}}, \omega_j) \alpha(\omega_{\mathbf{q}}), \tag{D.2}$$

$$b_{\mathbf{k}} = \sum_{\mathbf{q}} \nu^*(\omega_{\mathbf{q}}, \omega_{\mathbf{k}}) \alpha(\omega_{\mathbf{q}}). \tag{D.3}$$

Substituting Eqn. (D.1) into the eigenoperator relation, one ends up with a pair of equations

$$\mu(\omega_{\mathbf{q}}, \omega_j)(\omega_{\mathbf{q}} - \omega_j) = \sum_{\mathbf{k}} \nu(\omega_{\mathbf{q}}, \omega_{\mathbf{k}}) W_{\mathbf{k}j} \tag{D.4}$$

$$\nu(\omega_{\mathbf{q}}, \omega_{\mathbf{k}})(\omega_{\mathbf{q}} - \omega_{\mathbf{k}}) = \sum_j \mu(\omega_{\mathbf{q}}, \omega_j) W^*_{\mathbf{k}j} \tag{D.5}$$

which can be solved self-consistently to obtain $\omega_{\mathbf{q}}$. Using Eqn. (D.5), ν can be

expressed in terms of μ as

$$\nu(\omega_{\mathbf{q}},\omega_{\mathbf{k}}) = \left(\frac{\mathbb{P}}{\omega_{\mathbf{q}}-\omega_{\mathbf{k}}} + \delta(\omega_{\mathbf{q}}-\omega_{\mathbf{k}})z(\omega_{\mathbf{q}})\right)\sum_j \mu(\omega_{\mathbf{q}},\omega_j)W^*_{\mathbf{k}j} \tag{D.6}$$

where $\mathbb{P}$ stands for the principal part, and the δ-function term accounts for the contribution from the singularity. Inserting Eqn. (D.6) into Eqn. (D.4), the following relation for $\mu(\omega_{\mathbf{q}},\omega_j)$ and $z(\omega_{\mathbf{q}})$ is obtained.

$$\begin{aligned}\mu(\omega_{\mathbf{q}},\omega_j)(\omega_{\mathbf{q}}-\omega_j) &= \sum_{\mathbf{k}l}\frac{\mathbb{P}}{\omega_{\mathbf{q}}-\omega_{\mathbf{k}}}\mu(\omega_{\mathbf{q}},\omega_l)W_{\mathbf{k}j}W^*_{\mathbf{k}l} \\ &+ \sum_{\mathbf{k}l}\delta(\omega_{\mathbf{q}}-\omega_{\mathbf{k}})z(\omega_{\mathbf{q}})\mu(\omega_{\mathbf{q}},\omega_l)W_{\mathbf{k}j}W^*_{\mathbf{k}l}\end{aligned} \tag{D.7}$$

If we consider the nano-particle to have a single mode, the relation between μ and z can be written in a much simpler form and the dissipation of each mode can be treated separately. From this point on, we will use a subscript j where necessary denoting that we are working on the dynamics of the j^{th} mode of the nano-particle.

Relying on the above reasoning, $z_j(\omega_{\mathbf{q}})$ can be expressed as

$$z_j(\omega_{\mathbf{q}}) = \frac{\omega_{\mathbf{q}}-\omega_j-\sigma_j(\omega_{\mathbf{q}})}{g(\omega_{\mathbf{q}})|W_{\mathbf{q}j}|^2} \tag{D.8}$$

$\sigma_j(\omega_{\mathbf{q}})$ being the shift in the j^{th} nano-particle mode

$$\sigma_j(\omega_{\mathbf{q}}) = \mathbb{P}\int \frac{d\omega_{\mathbf{k}}\, g(\omega_{\mathbf{k}})|W_{\mathbf{k}j}|^2}{\omega_{\mathbf{q}}-\omega_{\mathbf{k}}}. \tag{D.9}$$

In order to obtain the expansion coefficients μ, ν phononic commutation relation for $\alpha(\omega_{\mathbf{q}})$ is employed.

$$[\alpha(\omega_{\mathbf{q}}),\alpha^+(\omega_{\mathbf{q}'})] = \delta_{\mathbf{q},\mathbf{q}'} = \frac{\delta(\omega_{\mathbf{q}}-\omega_{\mathbf{q}'})}{g(\omega_{\mathbf{q}})} \tag{D.10}$$

Using the expansion in terms of bare operators (D.1), and Poincare's theorem, i.e.

$$\begin{aligned}\frac{\mathbb{P}}{\omega_{\mathbf{q}}-\omega_{\mathbf{k}}}\cdot\frac{\mathbb{P}}{\omega_{\mathbf{q}'}-\omega_{\mathbf{k}}} &= \frac{\mathbb{P}}{\omega_{\mathbf{q}'}-\omega_{\mathbf{q}}}\left(\frac{\mathbb{P}}{\omega_{\mathbf{q}}-\omega_{\mathbf{k}}}-\frac{\mathbb{P}}{\omega_{\mathbf{q}'}-\omega_{\mathbf{k}}}\right) \\ &+ \pi^2\delta(\omega_{\mathbf{q}}-\omega_{\mathbf{k}})\delta(\omega_{\mathbf{q}'}-\omega_{\mathbf{k}}),\end{aligned} \tag{D.11}$$

the modulus square of $\mu(\omega_{\mathbf{q}}, \omega_j)$ is found as

$$|\mu(\omega_{\mathbf{q}}, \omega_j)|^2 = \frac{|W_{\mathbf{q}j}|^2}{(\omega_{\mathbf{q}} - \omega_j - \sigma_j(\omega_{\mathbf{q}}))^2 + \pi^2 g^2(\omega_{\mathbf{q}})|W_{\mathbf{q}j}|^4} \tag{D.12}$$

Since the Hamiltonian is diagonal with annihilation, creation operators $\alpha(\omega_{\mathbf{q}})$, $\alpha^+(\omega_{\mathbf{q}})$ and eigenfrequencies $\omega_{\mathbf{q}}$, the time dependence of the dressed annihilation operator is

$$\alpha(\omega_{\mathbf{q}}, t) = \mu(\omega_{\mathbf{q}}, \omega_j) a_j e^{-i\omega_{\mathbf{q}} t} + \sum_{\mathbf{k}} \nu(\omega_{\mathbf{q}}, \omega_{\mathbf{k}}) b_{\mathbf{k}} e^{-i\omega_{\mathbf{q}} t} \tag{D.13}$$

Correspondingly, the time dependence of the nano-particle annihilation operator reads (cf. Eqn. (D.2))

$$a_j(t) = \int d\omega_{\mathbf{q}}\, g(\omega_{\mathbf{q}})\, \mu^*(\omega_{\mathbf{q}}, \omega_j)\, \alpha(\omega_{\mathbf{q}})\, e^{-i\omega_{\mathbf{q}} t}. \tag{D.14}$$

Appendix E

A Note on the Non-Equilibrium Formulation of the Dissipation Problem

In this appendix, the dissipation problem for the systems strongly out of equilibrium is formulated. We follow system in contact with a reservoir approach, so that a temperature difference is created between the hot region (the system) and the remaining part which acts as a heat reservoir in contact with it. The initial temperatures of the system and the reservoir, internal degrees of freedom of the system, and that of the reservoir are the key ingredients of the problem. In Chapter 3, we have studied the problem for a nano-structure weakly coupled to a substrate for the near equilibrium case, where it is found that vibrational spectrum of the system affects the decay rates of individual modes together with the phonon density of states of the reservoir in a joint manner. Also it was shown that the time dependent occupations are linearly dependent to the initial excitations for near-equilibrium systems in the weak coupling regime whereas stronger coupling induces enhancements and retardations due to the reservoir mediated indirect coupling of the system modes. For non-equilibrium systems, however, the decay rates are expected to depend on not only the temperature difference but the effect 'background temperature' should be investigated as well.

In this appendix, we demonstrate that by using of Keldysh-Green functions [75] one can include the non-equilibrium effects in the results. Due to the phase coherence of the carries in nanometer scale the Keldysh-Green functions found a wide range of applicability in electronic and spintronic transport phenomena and gave results in good agreement with experiments [76]. The Keldysh-Green formalism has also been adopted to study steady-state phonon transport problem and it was shown that phononic transport displays quantum features which are similar to the effects found in the quantized electrical conductance [77]. Here we extend this approach to study the transient aspects of the phononic dissipation. By taking the advantage of Keldysh-Green functions, by which one can include many-body interactions on an equal footing with coupling to the reservoir, it also allows one to investigate the diffusive effects due to multi-phonon processes.

We first consider the system within the harmonic approximation in which the total Hamiltonian can be diagonalized as $H = \sum_{\mathbf{k},\lambda} \hbar\omega_{\mathbf{k}\lambda}(b^\dagger_{\mathbf{k}\lambda} b_{\mathbf{k}\lambda} + 1/2)$. Here $b_{\mathbf{k}\lambda}$, $b^\dagger_{\mathbf{k}\lambda}$ are the annihilation, creation operators corresponding to the eigenmode of the phonon branch λ with wavevector $\mathbf{k}$. In order to be able to define two different temperatures on a single surface, we need two sets of eigenmodes which are occupied according to two Bose-Einstein distributions separately. To set this, we use a fictitious partitioning scheme. That is, we consider the hot region as a free standing cluster of atoms keeping the atomic distances and the interactions the same with that of the periodic crystal. Diagonalizing the Hamiltonian for the cluster degrees of freedom, we obtain the vibrational modes of the cluster with frequencies ω_s. Using such a partitioning, we employ two complete basis sets for a single crystal, but we are able to define a system and a reservoir with this approach. One should note that the total Hamiltonian is still identical to the previous one. The interaction Hamiltonian between the system and the reservoir contain both sets of indices $\{\mathbf{k}, \lambda\}$ and $\{s\}$. The time-dependent non-equilibrium occupancies of the system modes are obtained using the correlation function as $\langle n_s(t)\rangle = iG^<_{s,s}(t,t)$, where the correlation function is defined as $G^<_{s,s'}(t,t') = -i\langle a^\dagger_{s'}(t')a_s(t)\rangle$, $a_s(t)$ being the annihilation operator for the ω_s mode of the system written in the Heisenberg picture. The correlation function

finds its expression within the Keldysh equation

$$\begin{aligned}\mathbf{G}^{<}(t,t') = \mathbf{g}^{<}(t,t') &+ \int_0^t dt_1 \int_0^{t_1} dt_2\, \mathbf{G}^{R}(t,t_1)\boldsymbol{\Sigma}^{R}(t_1,t_2)\mathbf{g}^{<}(t_2,t') \\ &+ \int_0^t dt_1 \int_0^{t_1} dt_2\, \mathbf{g}^{<}(t,t_1)\boldsymbol{\Sigma}^{A}(t_1,t_2)\mathbf{G}^{A}(t_2,t') \\ &+ \int_0^t dt_1 \int_0^{t_1} dt_2\, \mathbf{G}^{R}(t,t_1)\boldsymbol{\Sigma}^{<}(t_1,t_2)\mathbf{G}^{A}(t_2,t') \\ + \int_0^t dt_1 \int_0^{t_1} dt_2 \int_0^{t_2} dt_3 \int_0^{t_3} dt_4\, &\mathbf{G}^{R}(t,t_1)\boldsymbol{\Sigma}^{R}(t_1,t_2)\mathbf{g}^{<}(t_2,t_3)\boldsymbol{\Sigma}^{A}(t_3,t_4)\mathbf{G}^{A}(t_4,t') \quad \text{(E.1)}\end{aligned}$$

where $\mathbf{G}^{R(A,<)}$ are the matrices for retarded, advanced and lesser Green functions, $\mathbf{g}^{R(A,<)}$ and $\boldsymbol{\Sigma}^{R(A,<)}$ are the corresponding free Green functions and the self energies respectively. The retarded and advanced Green functions are obtained using the Dyson equation

$$\mathbf{G}^{R(A)}(t,t') = \mathbf{g}^{R(A)}(t,t') + \int_0^t dt_1 \int_0^{t_1} dt_2 \mathbf{G}^{R(A)}(t,t_1)\boldsymbol{\Sigma}^{R(A)}(t_1,t_2)\mathbf{g}^{R(A)}(t_2,t') \quad \text{(E.2)}$$

together with the following expression for the self energies

$$\boldsymbol{\Sigma}^{R(A,<)}_{s_1,s_2}(t_1,t_2) = \sum_{\mathbf{k}\lambda} V^{*}_{\mathbf{k}\lambda,s_1}\, g^{R(A,<)}_{\mathbf{k}\lambda}(t_1,t_2)\, V_{\mathbf{k}\lambda,s_2}. \quad \text{(E.3)}$$

The above system of equations are to be solved numerically by discretizing the time variables and using a finite mesh for the the reservoir density of states. The contributions of anharmonic effects to the self energy expressions are to be calculated using the diagrammatic technique [75].

Having obtained the time dependent occupations, one can calculate the transient energy of the system therefore the decay rates of the system modes. In the ballistic regime, the decay of individual system modes do not follow a common decrease of the system temperature. In fact there does not exist a well-defined temperature for such transient phenomena, rather each vibrational mode reaches

to equilibrium with the reservoir independently as it was the case in Chapter 3. On the other hand, the inclusion of anharmonic terms relates the decay rates of individual modes. In other words, the anharmonicity induced diffusive effect can be expected to enable us to define a unique system temperature during the transient process.

Bibliography

[1] K. S. Novoselov, A. K. Geim, S. V. Morozov, D. Yiang, Y. Zhang, S. V. Dubonos, I. V. Grigorieva, A. A. Firsov, Science **306**, 666 (2004).

[2] M. I. Katsnelson, K. S. Novoselov, A. K. Geim, Nature Physics **2**, 620 (2006).

[3] A. K. Geim and K. S. Novoselov, Nature Mater. **6**, 183 (2007).

[4] K. S. Novoselov, A. K. Geim, S. V. Morozov, D. Jiang, M. I. Katsnelson, I. V. Grigorieva, S. V. Dubonos and A. A. Firsov, Nature **438**, 197 (2005); Y. Zhang, Y.-W. Tan, H. L. Stormer and P. Kim, Nature **438**, 201 (2005).

[5] F. Schedin, A. K. Geim, S. V. Morozov, E. W. Hill, P. Blake, M. I. Katsnelson and K. S. Novoselov, Nature Mater. **6**, 652 (2007).

[6] T. B. Martins, R. H. Miwa, A. J. R. da Silva, A. Fazzio, Phys. Rev. Lett. **98**, 196803 (2007).

[7] M. Topsakal, H. Sevinçli and S. Ciraci, App. Phys. Lett. **92** 173118 (2008).

[8] Y.-W. Son, M. L. Cohen and S. G. Louie, Nature **444**, 347 (2006) (see also erratum: Nature.**446**, 342 (2007))

[9] Y.-W. Son, M. L. Cohen and S. G. Louie, Phys. Rev. Lett. **97**, 216803 (2006) (see also erratum: Phys. Rev. Lett. **98** 089901(E) (2007)).

[10] E. Rudberg, P. Salek and Y. Luo, Nano Lett. **7**, 2211 (2007).

[11] J. Nilsson, A. H. Castro Neto, F. Guinea and N. M. R. Peres, Phys. Rev. B **76**, 165416.

[12] X. Wang, Y. Ouyang, H. Wang, J. Guo and H. Dai, Phys. Rev. Lett. **100**, 206803 (2008).

[13] H. Sevinçli, M. Topsakal and S. Ciraci, (submitted for publication in Nanoletters) [arXiv:0711.2414].

[14] C.H. Xu, et al. J. Phys.: Condens. Matter **4**, 6047 (1992).

[15] G. W. Semenoff, Phys. Rev. Lett. **53**, 2449 (1984).

[16] M. Fujita, K. Wakabayashi, K. Nakada and K. Kusakabe, J. Phys. Soc. Jpn. **65**, 1920 (1996).

[17] L. Pisani, J. A. Chan, B. Montanari, N. M. Harrison, Phys. Rev. B **75**, 064418 (2007).

[18] K. Nakada, M. Fujita, G. Dresselhaus and M. S. Dresselhaus, Phys. Rev. B **54**, 17954 (1996).

[19] Y. Miyamoto, K. Nakada and M. Fujita, Phys. Rev. B **59**, 9858 (1999).

[20] M. Ezawa, Phys. Rev. B **73**, 045432 (2006)

[21] W. Kohn and L. J. Sham. Phys. Rev. **140**, A1133 (1965); P. Hohenberg and W. Kohn. Phys. Rev. B **76**, 6062 (1964).

[22] E. H. Lieb, Phys. Rev. Lett. **62**, 1201 (1989).

[23] L.Yang, C-H Park, Y-W Son, M. L. Cohen and S. G. Louie, Phys. Rev. Lett. **99**, 186801 (2007)

[24] R. A. de Groot, F. M. Mueller, P. G. van Engen, and K. H. J. Buschow, Phys. Rev. Lett. **50**, 2024 (1983).

[25] W. E. Pickett and J. S. Moodera, Phys. Today **54**, 39 (2001).

[26] G. Kresse, J. Hafner, Phys Rev. B **47**, 558 (1993); G. Kresse, J. Furthmuller, Phys Rev. B **54**, 11169 (1996).

[27] P. E. Blöchl, Phys. Rev. B **50**, 17953 (1994).

[28] L. Esaki and L. L. Chang, Phys. Rev. Lett. **33**, 495 (1974).

[29] X. Li, X. Wang, L. Zhang, S. Lee, and H. Dai, Science **319**, 1229 (2008).

[30] J. F.-Rossier, and J. J. Palacios, Phys. Rev. Lett. **99**, 177204 (2007).

[31] Claire Berger, Zhimin Song, Xuebin Li, Xiaosong Wu, Nate Brown, Cecile Naud, Didier Mayou, Tianbo Li, Joanna Hass, Alexei N. Marchenkov, Edward H. Conrad, Phillip N. First, Walt A. de Heer, Science **312**, 1191 (2006).

[32] M. -Y. Han, B. Özyilmaz, Y. Zhang, and P. Kim, Phys. Rev. Lett. **98**, 206805 (2007).

[33] B. Özyilmaz, P. J. -Herrero, D. Efetov, and P. Kim, App. Phys. Lett. **91**, 192107 (2007).

[34] R. Landauer, Philosophical Magazine **21**, 863 (1970).

[35] S. Datta, *"Electronic Transport in Mesoscopic Systems"*, (Cambridge University Press, Cambridge, 1995).

[36] M. Brandbyge, J.-L.Mozos, P. Ordejón, J. Taylor, K. Stokbro, Phys. Rev. B **65**, 165401, 2002.

[37] D. Fisher and P. Lee, Phys. Rev. B **23**, 6851 (1981).

[38] S. Tongay, R. T. Senger, S. Dag, S. Ciraci, Phys. Rev. Lett. **93**, 136404, (2004)

[39] *Physics of Sliding Friction*, Vol. 311 of *NATO Advanced Studies Institute, Series E, Applied Sciences*, edited by B. N. J. Persson and E. Tosatti (Kluwer, Dordrecht, 1996)

[40] *Micro/Nanotribology and its Applications*, Vol. 330 of *NATO Advanced Studies Institute, Series E, Applied Sciences*, edited by B. Bhuhan (Kluwer, Dordrecht, 1997)

[41] G. A. Tomlinson, Philos. Mag. **7**, 905 (1929)

[42] J. Frenkel and T. Kontorova, Phys. Z. Sowjetunion **13**, 1 (1938).

[43] B. Bhushan, J. N. Israelachvili, and U. Landman, Nature (London) **347**, 607 (1995).

[44] A. P. Sutton and J. B. Pethica, J. Phys.: Condens. Matter **2**, 5317 (1990).

[45] J. A. Nieminen, A. P. Sutton, and J. B. Pethica, Acta Metall. Mater. **40**, 2503 (1992).

[46] M. R. Sorensen, K. W. Jacobsen, and P. Stoltze, Phys. Rev. B **53**, 2101 (1996)

[47] M. R. Sorensen, K. W. Jacobsen, and H. Jonsson, Phys. Rev. Lett. **77**, 5067 (1996).

[48] A. Buldum and S. Ciraci, Phys. Rev. B **55**, 2606 (1997).

[49] A. Buldum and S. Ciraci, Phys. Rev. B **55**, 12892 (1997).

[50] A. Buldum, S. Ciraci, and I.P. Batra, Phys. Rev. B **57**, 2468 (1998).

[51] W. Zhong and D. Tomanek, Phys. Rev. Lett. **64**, 3054 (1990).

[52] D. Tomanek, W. Zhong, and H. Thomas, Europhys. Lett. **15**, 887 (1991).

[53] M. Cieplak, E. D. Smith, and M. O. Robins, Science **265**, 1209 (1994).

[54] E. D. Smith, M. O. Robbins, and M. Cieplak, Phys. Rev. B **54**, 8252 (1996).

[55] J. B. Sokoloff, Phys. Rev. B **42**, 760 (1990).

[56] J. B. Sokoloff, Phys. Rev. B **42**, 6745(E) (1990).

[57] J. B. Sokoloff, Phys. Rev. B **51**, 15573 (1995).

[58] J. B. Sokoloff, Phys. Rev. Lett. **71**, 3450 (1993).

[59] A. Buldum and S. Ciraci Phys. Rev. B **60**, 1982 (1999)

[60] A. Buldum, D. M. Leitner, and S. Ciraci Phys. Rev. B **59**, 16042 (1999)

[61] A. Buldum, S. Ciraci, and I. P. Batra Phys. Rev. B **57**, 2468 (1998)

[62] A. Erdemir et al., J. Vac. Sci. Technol. A **18**, 1987 (2000).

[63] H. Sevincli, S. Mukhopadhyay, R. T. Senger, and S. Ciraci, Phys. Rev. B **76**, 205430 (2007).

[64] S. M. Barnett and P. M. Radmore, *"Methods in Theoretical Quantum Optics"*, (Oxford University Press, 1997).

[65] U. Fano, Phys. Rev. **124**, 1866 (1961).

[66] P. W. Anderson, Phys. Rev. **124**, 41 (1961).

[67] G. D. Mahan, *"Many-Particle Physics"*, (3rd ed.) (Kluwer Academic/Plenum Publishers, New York, 2000)

[68] As long as $(\omega_j/\Gamma) \gg 1$ and $(\omega_D/\Gamma) \gg 1$ the Lorentzian is localized into the range where the Debye-DOS is finite, so no extra contribution raises with extending the limits of integration.

[69] B. N. J. Persson, A. I. Volokitin, *Physics of Sliding Friction*, Vol. 311 of *NATO Advanced Studies Institute, Series E, Applied Sciences*, edited by B. N. J. Persson and E. Tosatti, (Kluwer, Dordrecht, 1996), pp. 253-264.

[70] D. Vanderbilt, Phys. Rev. B **41**, R7892 (1990).

[71] J. P. Perdew, K. Burke, and M. Ernzerhof, Phys. Rev. Lett. **77**, 3865 (1996).

[72] J. P. Perdew, J. A. Chevary, S. H. Vosko, K. A. Jackson,M. R. Pederson, D. J. Singh, C. Fiolhais, Phys. Rev. B **46**, 6671 (1992).

[73] M. P. Lopez-Sancho, J.M. Lopez-Sancho, and J. Rubio, J. Phys. F **14**, 1205 (1984).

[74] M. B. Nardelli, Phys. Rev. B **60**, 7828 (1999).

[75] L. V. Keldysh, Zh. Eksp. Theor. Fiz **47**, 1515 (1964), [Sov. Phys. JETP **20**, 1018 (1965)].

[76] H. Haug and A.-P. Jauho, *Quantum Kinetics in Transport and Optics of Semiconductors*, Springer Solid State Sciences, Vol. 123 (Springer-Verlag, Berlin, 1996).

[77] A. Özpineci and S. Ciraci, Phys. Rev. B **63**, 125415 (2001).